Investigation on the Influence of Organic Polymer Additives on n-Heptane Autoignition

A Thesis
SUBMITTED TO THE FACULTY OF
UNIVERSITY OF MINNESOTA
BY

Kali Ann Johnson

IN PARTIAL FULFILLMENT OF THE REQUIREMENTS
FOR THE DEGREE OF
MASTER OF SCIENCE

Dr. William Northrop

December 2016

Acknowledgements

I would like to acknowledge Dr. William Northrop for his encouragement, support, and guidance throughout this project. I would also like to thank Xuesong (Sean) Li for his assistance while I conducted the experiments for this work. His technical knowledge and support was instrumental in the success of this project. I would also like to thank Dr. Marc Hillmyer and Annabelle Watts from the Center for Sustainable Polymers at the University of Minnesota. Their expertise helped immensely with the chemistry aspect of this project, and their support helped form a successful collaboration between our two organizations. In addition, I would like to recognize Cecilia Hall for her patience and generosity in setting aside time from her schedule to assist me with my project. I would also like to thank Darrick Zarling for providing guidance with the experimental setup for this work. Lastly, I would like to thank Andrew Kotz for his mentorship and guidance throughout my graduate career.

Abstract

Increasing compression ratio of spark ignition (SI) engines can improve fuel efficiency; however, engines with higher compression ratios are more likely to experience knock or pre-ignition, a potentially damaging phenomenon. One method to suppress knock is to use fuel additives; however, traditional organometallic additives like tetraethyl lead, while effective create toxic lead oxide nanoparticles. This study examined the hypothesis that organic polymer nanoparticles could be used as environmentally benign anti-knock additives by scavenging gas-phase radicals responsible for autoignition and then be consumed in the eventual combustion event. The organic polymer polycyclohexylethylene (PCHE) in n-heptane, a single component gasoline fuel surrogate, was experimentally investigated. To imitate fuel atomization and vaporization in a SI engine, a pneumatic atomizer was used to generate PCHE nanoparticles entrained in gaseous n-heptane and air mixtures. Liquid phase concentrations of 0.01, 0.05 and 0.10 percent by weight PCHE in n-heptane were compared to n-heptane with no additive. Particle number as a function of diameter produced by the atomization process was quantified for each solution. In addition, the thermal stability and autoignition characteristics of the additive-doped fuels were examined using a laminar flow reactor.

Results of the study showed that the pneumatic atomization process was able to successfully produce solid PCHE nanoparticles. Number of particles increased with additive concentration indicating that the PCHE was miscible in liquid n-heptane. Thermal

degradation of the PCHE nanoparticles began when the reactor temperature reached approximately 775 ˚C. Although droplet evaporation produced PCHE nanoparticles in significant concentrations, the reactive experiments showed no difference in autoignition temperature between the additive-containing fuels and n-heptane alone. Although the central hypothesis of the study was not proven for PCHE particles, the same experimental design can be tested with other organic polymers.

Table of Contents

List of Tables

List of Figures

1 Introduction

Spark ignition (SI) engines used in light-duty vehicles account for approximately 44% of US oil consumption.[1] As light-duty vehicle ownership increases, demand on the world's energy resources also grows. In addition, combustion products from SI engines negatively impact the environment, including contributing to the rise in global atmospheric CO_2 concentration.[2] In order to more fully investigate and address these underlying concerns, research and development that focus on minimizing fuel consumption and mitigating environmental impacts from SI engines are necessary.

One approach for reducing fuel consumption in SI engines is to increase their compression ratio (ratio of largest to smallest volume inside the engine's combustion chamber). Decreasing fuel consumption leads to lower CO_2 emissions.[1] However, efficient, high compression ratio engines require fuels that are more resistant to autoignition than today's fuels. The octane number is the measure of a gasoline's tendency to resist knock. Historically, fuel additives like tetraethyl lead (TEL) have been used to increase a fuel's octane rating.[2,3] However, TEL and other organometallic additives have been banned due to the toxic nanoparticles emitted when they are combusted. Therefore, a new, environmentally benign additive to increase gasoline octane number is needed.

The work presented in this thesis describes a novel solution to raise the octane number of gasoline through the use of an organic polymer nanoparticle additive. Organic polymer nanoparticles, if they could be developed to have gas-phase radical inhibiting

characteristics like TEL, are an ideal additive because they are combusted after they act to inhibit autoignition, resulting in no byproduct emissions. In addition, organic polymers can be synthesized in organic solvents, a characteristic that is ideal for miscibility with gasoline. No known research is available that investigates using organic polymer nanoparticles as fuel octane additives.

1.1 Research Objectives

The overarching hypothesis motivating this study is that polymer nanoparticles formed during evaporation of fuel sprays can influence autoignition of fuel and air mixtures through radical scavenging via adsorption. The experimental work described in this thesis represents a first step to test this hypothesis and to explore potential mechanisms by which organic polymer nanoparticles act as fuel additives. The capability of organic polycyclohexylethylene (PCHE) polymer nanoparticles to hinder autoignition of single component gasoline surrogate fuels is studied. The primary objectives of the experimental study described in this thesis was to: (1) characterize the size and concentration of nanoparticles formed through fuel droplet evaporation, (2) quantify the thermal degradation properties of the PCHE nanoparticles using a laminar flow reactor, and (3) measure autoignition temperatures of n-heptane with and without the PCHE additive. This research takes the first step to developing an environmentally benign fuel additive to increase the octane number rating of gasoline.

1.2 Background

Ignition in Spark Ignition Engines and Engine Knock

There are four primary cycles of operation in a four-stroke SI engine. During the first cycle, the piston moves towards bottom dead center and a mixture of fuel vapor and air enter the cylinder through an intake valve. Next, the intake valve closes, and the piston moves towards top dead center, which compresses the fuel air mixture inside the cylinder. The third cycle is known as the power stroke. During the power stroke, a spark creates a small high temperature flame kernel where a larger turbulent premixed flame propagates through the remaining unburned mixture.[4] The unburned mixture is consumed by the flame and the fuel air mixture ignites driving the piston towards the bottom of the cylinder. Lastly, an exhaust valve opens and the piston moves back towards top dead center to push the combustion products out of the chamber.

A serious limitation in SI engines is the tendency of the unburned gas to autoignite before being consumed by the flame front. This phenomenon is known as engine knock and causes temperatures and pressures to spike in the combustion chamber. Knock decreases engine performance and can destroy the combustion chamber walls and/or piston. The cause of knock varies; for example, hot spots on the cylinder wall due to carbon deposits can cause the mixture to spontaneously ignite, causing knock (Figure 1).[4] In addition, knock can occur if the temperature and pressure inside the combustion chamber are elevated enough to cause the fuel to spontaneously autoignite. Knock predominantly

occurs at high engine loads due to elevated in-cylinder temperature and at low engine speed, where sufficient time is available for autoignition chemistry.

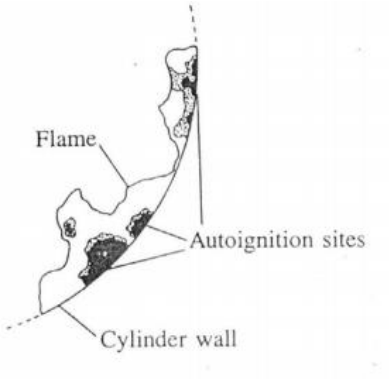

Figure 1: Autoignition sites in the end gas along the cylinder wall (Figure from Internal Combustion Engine Fundamentals)[3]

Knock is primarily controlled in modern SI engines by keeping compression below 12:1 in engines without intake boosting and below 10:1 in engines with turbocharging. Decreasing the compression ratio mitigates knock because lower pressure and temperature inside the combustion chamber prevent the fuel from autoigniting. However, decreasing the compression ratio has adverse effects on engine performance, especially for high load efficiency and torque capability.[5,6] Thermodynamically, engine efficiency decreases with decreasing compression ratio. Thermal efficiency is defined as the percentage of thermal energy input to the engine that is converted to mechanical work.[7] As shown in Equation 1.1, thermal efficiency (η_T), is directly related to the compression ratio (CR) for the ideal air standard Otto Cycle, an idealized representation of the closed portion of real engine cycles[6]:

$$\eta_T = 1 - \left(\frac{1}{CR}\right)^{\gamma-1} \quad \textbf{(1.1)}$$

In the equation, γ is the ratio of constant pressure specific heat to constant volume specific heat of the gas. This equation assumes the compression and expansion process are adiabatic and reversible (isentropic). It should be noted that for the ideal air standard Otto Cycle, the thermal efficiency is dependent on the compression ratio for the extent that γ depends on the compression ratio.[3]

Retarding spark timing is another method used to control engine knock. Spark timing is the location, in crank angle degrees before top dead center that the spark plug initiates a flame front in the combustion chamber. Spark timing is optimized to obtain the highest efficiency and best torque output based on engine parameters like engine speed and fuel-air ratio.[4] Usually the spark plug is initiated before the piston reaches top dead center, meaning the gas has not been fully compressed. Advancing the spark ensures that the fuel air mixture is entirely consumed during the power stroke resulting in the highest efficiency. Conversely, early ignition causes the peak pressure and temperature to increase. If the pressure and temperature become too elevated, engine knocking can occur. Thus to prevent engine knocking, spark timing must be retarded and will no longer be optimized,[8] resulting in reduced torque and efficiency.

Research and Motor Octane Number

A measure of a gasoline's tendency to resist knock is the octane number. Fuels with high octane numbers enable engines to have higher compression ratios, resulting in improved engine efficiency. Increasing engine efficiency is essential to decrease the environmental footprint of SI engines. By 2025, EPA's greenhouse gas regulations will require all passenger cars, light-duty trucks, and medium-duty passenger vehicles to have a fleet average industry standard of 54.5 miles per gallon and emit only 163 grams per mile of CO_2.[9]

The octane number is a metric based on the ignition tendency of a fuel compared to two reference fuels, n-heptane and iso-octane that have octane numbers of 0 and 100, respectively. The smaller the octane number, the more likely the fuel is to knock. Octane numbers are tested in an ASTM Cooperative Fuel Research Engine (CFR) which is a single cylinder variable compression ratio engine. There are two standardized octane tests using the CFR engine that give two octane numbers: the Research Octane Number (RON) and the Motor Octane Number (MON). The standard test method for RON and MON can be found in ASTM D2699 and ASTM D2700, respectively. The antiknock index (AKI), which is displayed at fuel dispensers in the United States, is the average of the RON and MON for a given fuel:[4,5]

$$AKI = \frac{RON + MON}{2} \quad \textbf{(1.2)}$$

The difference between RON and MON for a given fuel is known as the sensitivity:[5]

$$S = RON - MON \quad \textbf{(1.3)}$$

Although the CFR engine is used to determine the octane number for a given fuel according to the ASTM standards with or without an additive, it does not allow for controlled diagnostics to examine additive behavior or the ability to change temperature and pressure independently. Therefore, a more fundamental reactor was used in this work to test the use of PCHE as a fuel octane additive for SI engines.

Chemical Kinetics during Autoignition

Elevated pressure and temperatures promote the formation of radical species in the combustion chamber, which cause autoignition to occur. Radicals are chemically reactive molecules that have (an) unpaired electron(s) and are the primary cause of engine knock.[7] Pitz and Westbrook postulated that at elevated temperatures and pressures where the end gas tends to knock, autoignition was most responsive to reactions involving the production and consumption of the hydroperoxyl radical, HO_2, and hydrogen peroxide, H_2O_2.[10] In particular, HO_2 reacts with the fuel and promotes chain branching as shown in Equation 1.4.

$$C_xH_y + HOO\cdot \rightarrow C_xH_{y-1}\cdot + H_2O_2 \quad \textbf{(1.4)}$$

H_2O_2 will then decompose and promote chain branching to produce the hydroxyl radical, OH.[10]

$$H_2O_2 + M \rightarrow \cdot OH + \cdot OH + M \quad \textbf{(1.5)}$$

In the above equation, M is a non-participating third body molecule. When the pressure is near atmospheric and the temperature is greater than 1000 K, the chain branching reaction shown below dominates:

$$H + O_2 \rightarrow O + \cdot OH \quad \textbf{(1.6)}$$

However, this reaction is not as important in higher pressure systems like internal combustion engines.[10]

Controlling Engine Knock with Fuel Additives

Metal Oxides

In order to increase the octane rating of fuels and control radical formation in the end gas, various materials like alcohols, metal oxides and organic materials have been researched as potential fuel additives. Metal oxides including tetraethyl lead (TEL), ferrocene, and methylcyclopentadienyl manganese tricarbonyl (MMT) have proven to improve gasoline's tendency to autoignite. The most effective metal oxide fuel additive is tetraethyl lead (TEL) or $(C_2H_5)_4Pb$ which was discovered in 1922 by Midgely and Boyd.[4] Although it is a well-known octane additive, the radical inhibition mechanism of TEL is largely unknown. For example, there is no general consensus regarding the state of TEL in the end gas (solid or vapor).[10] TEL is soluble in gasoline and has the ability to modify chain reactions by decomposing in the end gas, oxidizing to form lead oxide, and reacting with radicals via surface reactions.[7,10] Surface reactions are likely because lead oxide has a

relatively small diameter ranging from 4-10 nm, resulting in a large total surface area and an efficient catalytic surface.[10] Due to its effective catalytic surface, the reactive species in the end gas form into unreactive products. The following chemical reactions are thought to take place[7]:

$$PbO + \cdot OH \rightarrow PbO(OH) \quad \textbf{(1.7)}$$

$$PBO(OH) + \cdot OH \rightarrow PbO_2 + H_2O \quad \textbf{(1.8)}$$

$$PbO_2 + \cdot R \rightarrow PbO + \cdot RO \quad \textbf{(1.9)}$$

In the above equation, R is a radical. Surface reaction rates are directly proportional to the species concentration. By decreasing the amount of reactive species present in the end gas, autoignition tendency decreases significantly. Through a simplified model with TEL as the fuel additive, Pitz and Westbrook found that by removing HO_2 and H_2O_2 from the end gas increased ignition delay by 31% compared to the base model with no additive. The model used n-butane and air in a constant volume reactor.[10]

Although metal oxide additives are very effective knock inhibitors, they are no longer used as fuel additives in the United States due to the environmental and public health risk they pose. For example, automotive lead exhaust has been linked with metabolic disorders, retardation in growth and development, hearing loss, and neurological deficits.[11] TEL also deactivates exhaust aftertreatment catalysts used to eliminate other harmful engine emissions like carbon monoxide, hydrocarbons and NO_X. Similarly, the metal oxide ferrocene has limited use as a fuel additive since ferrocene byproducts cause abnormal

electric discharge patterns on the spark plug. This causes defective ignition to occur and can destroy the spark plug over time.[12]

If purely organic additives could be used, they would ideally be oxidized during the main combustion process and result in no additional emissions like in the case of metal additives. Historically, the organic additives used in fuel have not been as effective as organo-metallic additives at increasing the octane rating. For example, aniline is only 3% as effective as TEL on a mass basis and has such a strong odor that it is no longer used in industry.[7] As a result of these unfavorable attributes, research on organic additives is limited. Current research is focusing on the use of biofuels and blending.

Biofuels

Biofuels can also be economical antiknock agents, though they require blending at higher concentrations than additives. Two biofuels that are particularity effective at mitigating knock are ethanol and methanol. Methanol has disadvantages in that it is acutely toxic to humans and animals, miscible in water, accelerates deteriorations of elastomers, and corrodes metals in the fuel system.[13]

Ethanol is also an effective knock inhibiter; pure ethanol has an RON of 109.[14] The United States is a large producer of fuel ethanol since it is derived from grains like corn.[15] Some have shown that gasoline blended with ethanol produces less benzene, volatile organic compounds, and particulate matter emissions than pure gasoline of an equivalent octane number rating.[16,2] Ethanol splash blended with 87 AKI gasoline at a level of 20%

(E20) has been shown to allow a higher compression ratio to be used due to its higher octane, thus reducing CO_2 emissions from a light duty vehicle by 5%.[14] However, ethanol also has environmental limitations. Production of corn-based ethanol has been shown to have questionable renewability depending on how land use is taken into account.[2] Some have also shown that ethanol impedes the biodegradation of petroleum contaminants, contributing to ground water contamination and soil severity.[2]

Organic Polymers and Nanoparticles

In contrast to metal additives, if an organic polymer could be synthesized to have anti-knock properties, they could be completely oxidized during combustion. Further, organic polymers can potentially be blended at very low concentrations (< 1000 ppm) in the fuel unlike ethanol that requires >10% splash blending for efficacy. Though organic polymers have not been used as fuel additives, they have shown radical scavenging functionality in other applications. For example, there are organic polymers that have the capability to scavenge free radicals formed in the body.[17] Free radical formation in the body is a natural process that relies on antioxidants such as porous polymers for neutralization. In addition, some organic polymers have high chemisorption and physisorption capabilities that are comparable to adsorbent materials like zeolites and metal organic framework materials.[18,19] Due to these capabilities, organic polymers can be used to capture gases, drug ingredients, and organic vapors.[18,20] High adsorption capabilities would be desirable in a fuel additive for capturing greenhouse gases formed during the

combustion process. In one study conducted by El-Kaderi *et al*., an organic polymer with high specific surface area was able to separate and capture carbon dioxide from flue and natural gas.[21] Properties like high surface area and potentially chemically reactive functionalities could be very attractive for fuel additives.

A subset of organic polymers that have characteristics similar to metal oxide fuel additives are organic polymer nanoparticles that range from 10-1000 nm in diameter. Polymer nanoparticle technology is quickly emerging into fields like pharmaceuticals, electronics, molecular imaging, and pollution control.[22–24] Organic polymer additives are of interest in this study because it is theorized that the nanoparticles created when additive-containing fuel droplets evaporate have large surface to volume ratio similar to TEL and have the potential to physisorb or chemisorb gas phase radicals. Also, their miscibility in surrogate fuels can be tuned by choosing specific chemistries. In addition, properties of nanoparticles can be synthetically altered to optimize the final properties. For example, when organic polymer nanoparticles are developed with a high degree of porosity, specific surface area significantly increases. Developing high porosity polymers may also increase gas adsorption capabilities if it is available kinetically.[25,26]

Although organic polymer nanoparticles have the potential to be radical scavengers in liquids, there is little knowledge about their capabilities for scavenging gas phase radicals. Further, their stability at elevated temperatures and pressures similar to ignition conditions in an SI engine has been largely unexplored. Thermal degradation of polymers

depends on multiple parameters including the heating rate and the atmosphere in which the polymer is suspended. It should be noted that for most polymers, an increase in the heating rate causes the polymer to thermally degrade faster.[27] Although the reasoning for this is unclear, it is surmised that the reaction mechanism of decomposition depends on the heating rate present and the heat transfer between the heating source and the polymers.[27]

The atmosphere under which degradation occurs has an effect on the polymer's degradation temperature. For example, a study done by J.D. Peterson *et. al* researched thermal degradation of polystyrene (PS) in nitrogen and air at a rate of 9.0 and 8.2 K/min, respectively. In the presence of an inert gas, nitrogen, PS started to thermally degrade at 250 ˚C and was completely degraded by 500 ˚C. However, in the presence of air, PS started to thermally degrade at 200 ˚C and finished degrading at 450 ˚C.[28] This can be rationalized by the presence of oxygen, which can participate in radical formation reactions that accelerate the degradation of the polymer backbone. Thus, any oxygen present in end gas prior to combustion may reduce the polymer stability. Pressure also has a direct effect on polymer thermal degradation. A study conducted by Murata *et.al*. found that decomposition rate and the proportions of degradation products were significantly affected by pressure. In particular, pressure affects the scission of the double bond C-C chains in polymers, and the molecular weight distribution of produts.[29] With higher pressure, the carbon number distribution of gaseous and liquid products and the molecular weight distribution of reactor contents shifted to the lower molecular weight side.

Although most polymers have established degradation temperatures in air or nitrogen, these do not directly translate to the behavior of these materials in an engine cylinder. Literature values for degradation temperature and proposed mechanisms are determined by subjecting the polymers to controlled, incremental heating rates. It should be noted that in an engine, a polymer additive could experience extremely high temperatures almost instantaneously. For example, at 600 rpm, an end gas might be exposed to temperature ranging from 450-900 K for a maximum of 40 ms.[30] The polymer needs to have high thermal stability to ensure that thermal decomposition does not occur before ignition so that the additive can actually be effective at scavenging radicals.

Polycyclohexylethylene

The polymer nanoparticle chosen for this study is polycyclohexylethylene (PCHE). PCHE is composed of only carbon-carbon and carbon-hydrogen single bonds, which are very stable to the mechanism of homolytic cleavage to generate radicals. This saturated hydrocarbon structure also imparts miscibility in both surrogate fuels, iso-octane and n-heptane, which are used in octane rating tests. PCHE originates from a commodity plastic, polystyrene (PS).[31] To obtain PCHE, PS is hydrogenated, removing the aromaticity in the side chain of the polymer. As it is sourced from a commodity plastic, and hydrogenation is a common reaction performed on industrial scales, PCHE could be produced cheaply on large scales. Table 1 provides the key properties of PCHE and PS. PCHE has relatively good rigidity and is environmentally stable at room temperature.[31] The glass temperature

(T_g) is higher for PCHE than PS.[31] When a polymer is exposed to temperatures above T_g, Brownian motion is present and the polymers flows; it does not indicate polymer degradation. A higher glass temperature is important because the polymer will be exposed to elevated temperatures in the combustion chamber, but it should be noted that the exposure duration is very short (ms).

Thermal stability of PCHE is a key property of interest in this study. Zhao *et al.* concluded that PCHE will start to thermally degrade at 280 ˚C when heated in a nitrogen atmosphere at a rate of 3 ˚C/min.[32] It is important to note that the temperature at which a polymer degrades will depend on the atmosphere the polymer is suspended in. There was no known research on the degradation of PCHE or PS in conditions similar to a SI engine's combustion chamber.

Table 1: PCHE and PS Properties[31]

Property	PCHE	PS
T_g (°C)	147	106
Density (g/cm^3)	0.947	1.06
Heat Capacity @ 25°C (J/gK°)	2.0	1.2

PCHE is developed from two major chemical processes: anionic polymerization of styrene and hydrogenation of polystyrene. First, styrene is anionically polymerized to form the polymer chain. This is done by breaking the carbon-carbon (C-C) pi bonds on two monomers and creating a new C-C single bond between the two monomers. Repeating this process gives the long chain hydrocarbon polystyrene as shown in Figure 2. The single C-

C bonds are very stable, making polystyrene relatively strong and difficult to decompose.[33] Subsequently following the polymerization, PS is saturated using heterogeneous catalytic hydrogenation.

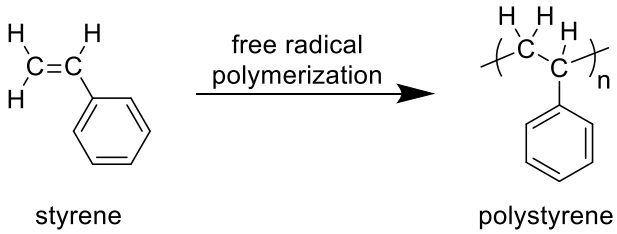

Figure 2: Styrene to Polystyrene mechanism[34]

There are three factors necessary for hydrogenation: an unsaturated substrate like PS, H_2 gas, and a catalyst. Depending on the catalyst and unsaturated substrate, a specific pressure and temperature are required to complete the hydrogenation process. During hydrogenation, the catalyst surface like $PdSiO_2$ will break apart the H_2 bond and saturate the organic compound. Heterogeneous hydrogenation is beneficial because the catalyst and material consists of two phases; therefore, the catalyst is not in solution and can be easily filtered out of the material.[33] After hydrogenation, the final product is PCHE as shown in Figure 3.

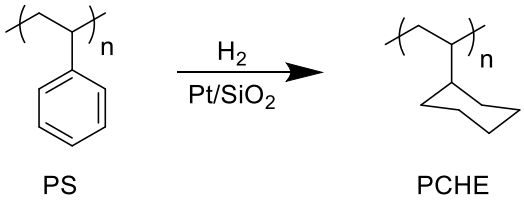

Figure 3: Hydrogenation of Polystyrene[31]

Fuel Atomization and Polymer Nanoparticle Formation

In gasoline engines, the fuel is pressurized and injected either directly into the combustion chamber or into the intake manifold just before the valves that let air into the cylinder. An illustration depicting a low-pressure gasoline fuel injector is shown in Figure 4. The injector simultaneously controls the fuel flow and atomizes the liquid fuel. In gasoline engines, the fuel is completely vaporized and mixed with the air in the cylinder before combustion begins.

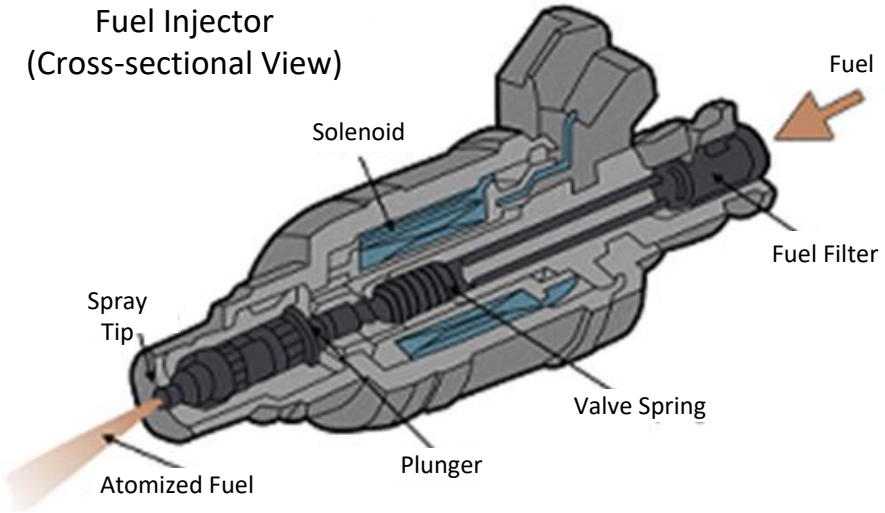

Figure 4: Cut through diagram of IC engine fuel injector[35]

To mimic fuel droplet evaporation in a gasoline spark ignition engine, this study used a pneumatic atomizer to produce suspended PCHE nanoparticles in a gaseous fuel and air mixture. It is hypothesized that following atomization, the single polymer nanoparticles coalesce as the liquid droplets evaporate, resulting in nanoparticles that consist of a large number of polymer molecules together. It is theorized that these

nanoparticles will contain some porosity and a specific surface area large enough to adsorb radicals. A graphical depiction of the theorized process is given in Figure 5.[36]

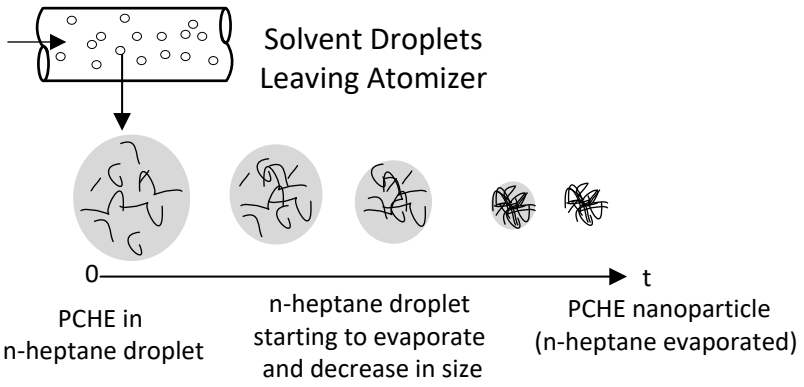

Figure 5: Visual representation showing the evaporation of the n-heptane after atomization (drawing not to scale)

The final size of the nanoparticles formed during the atomization process can be predicted from the volume fraction, F_v of the solute dissolved in the solvent[36]:

$$d_p = d_d(F_v)^{\frac{1}{3}} \quad \textbf{(1.10)}$$

In the above equation, the droplet diameter is d_d and the final solid particle diameter is d_p. The volume fraction of the solute dissolved in the solvent is determined by using Equation 1.11:

$$F_v = wt\% * \frac{\rho_{hep}}{\rho_{poly}} \quad \textbf{(1.11)}$$

In Equation 1.11, ρ_{hep} and ρ_{poly} is the density of the n-heptane and polymer, respectively. Equation 1.10 shows that for a given initial droplet size, solid particle diameter is directly correlated to the concentration of the solution; higher concentrations

give larger solid particles. For most atomizers, the initial droplet diameter can be varied by altering the atomizer pressure applied to the solution, which changes the shear force applied to the liquid solution during atomization.

Pneumatic atomization is fairly common in the pharmaceutical industry to increase a drug's bioavailability (effective portion of a substance). Bioavailability is hindered when pharmaceutical ingredients are poorly soluble, typically due to drug crystallization. To combat this issue, pharmaceutical companies will pair the drugs with biodegradable polymers that have optimal solubility characteristics via favorable interactions with the drugs, preventing crystallization. The suitable polymer and drug are combined with a solvent that dissolves both the drug and the polymer. After filtering, the drug and polymer solution is spray dried, using the same process as described above for atomization. The rapid evaporation of the solvent prevents drug crystallization as the polymer traps the drug in the amorphous state.[22] Thus by utilizing spray drying, the solubility of the drug is increased with respect to the original crystalline form.[37,38]

2 Experimental Methods and Procedures

2.1 Overview

Chapter 2 details a developed three sets of experiments to understand a polymer's characteristics as a fuel additive and meet the aforementioned project objectives using the organic polymer PCHE produced in cooperation with the University of Minnesota's

Chemistry Department. Although PCHE was chosen, the primary intent of this study was to develop a technique for measuring ignition delay for fuels with a range of polymer additives. When produced, PCHE is a solid, macroscopic crystal. The PCHE crystals were dissolved in the surrogate fuel n-heptane at various concentrations based on weight percent and atomized using a TSI 3076 atomizer that generated entrained PCHE nanoparticles.

In the first set of experiments, the size and concentration of PCHE nanoparticles generated *in situ* during atomization was determined. Next, the thermal degradation of the polymer was studied using a laminar flow reactor (LFR). Finally, the autoignition behavior of PCHE was collected. The fuel specifications for the two surrogate fuels used in this study, n-heptane and iso-octane, are shown below in Table 2.

Table 2: n-Heptane and Iso-Octane Fuel Specifications from Sigma Aldrich

Parameter	n-Heptane (anhydrous)	Iso-octane
Sigma Aldrich PN	246654	360066
Molecular Formula	$CH_3(CH_2)_5CH_3$	$(CH_3)_2CHCH_2C(CH_3)_3$
Molecular Weight (g/mol)	100.20	114.23
Upper Flammability Limit (% by volume of air)	7	6
Lower Flammability Limit (% by volume of air)	1.1	.79
Vapor Pressure	83 mmHg (at 37.7 °C)	41 mmHg (at 21 °C)
Relative Density (g/ml at 25 °C)	.68	0.69
Auto-ignition Temperature (°C)	223	396
Initial boiling point (°C)	98	98

2.2 *In situ* Generated PCHE Nanoparticle Formation via Atomization

Before collecting data for the three sets of experiments, different concentrations of PCHE were dissolved in n-heptane to produce approximately two liters of the following four solutions: 0.00, 0.01, 0.05, and 0.10 weight percent (wt %) of PCHE dissolved in n-heptane. The 0.00 wt % solution represents n-heptane with no fuel additive. Equation 2.1 provides the traditional weight percent equation, however the PCHE used in this study was solid requiring the use of a modified weight percent calculation shown in Equation 2.2. Each solution was stirred for approximately 24 hours to ensure that the PCHE was fully dissolved in the n-heptane.

$$\text{Wt \%} = \frac{V_{\text{Solute}} \times \rho_{\text{Solute}}}{V_{\text{Solute}} \times \rho_{\text{Solute}} + V_{\text{Heptane}} \times \rho_{\text{Heptane}}} \quad \textbf{(2.1)}$$

$$\text{Wt \%} = \frac{\text{Mass}_{\text{PCHE}}}{\text{Mass}_{\text{PCHE}} + V_{\text{Heptane}} \times \rho_{\text{Heptane}}} \quad \textbf{(2.2)}$$

As mentioned previously, a TSI 3076 pneumatic atomization was used to mimic fuel droplet evaporation in an SI engine, as shown in Figure 6.

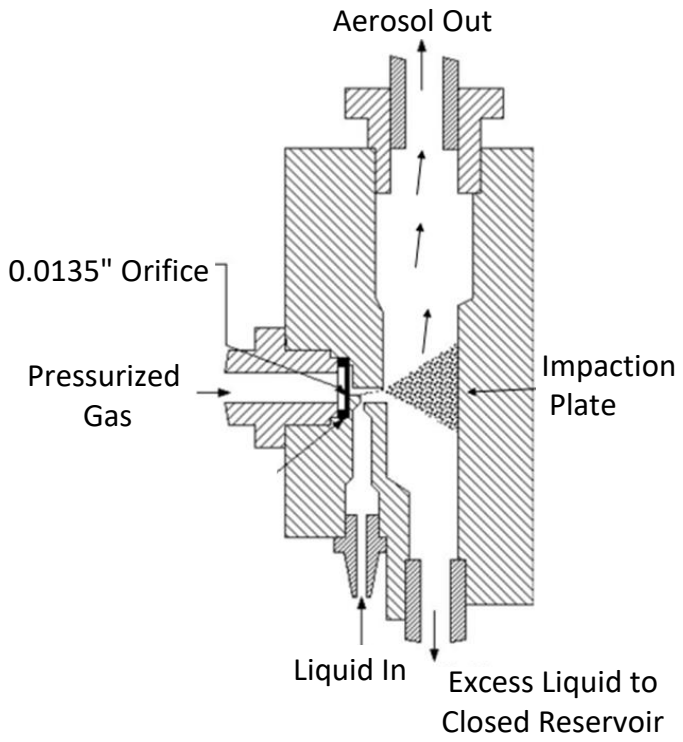

Figure 6:Cross-sectional view inside the TSI 3076 Atomizer demonstrating the atomization process (Figure from TSI 3076 Manual)

First, the test solution was collected in a Monoject syringe. The syringe was placed in a NE-1000 programmable syringe pump that was set to deliver a constant flowrate of 2 ml/min of solution to the atomizer. Simultaneously, filtered gas ranging from 25-35 psig entered the atomizer through a 0.0135" diameter orifice. The high velocity of the air created a pressure drop inside the atomizer. As a result of the Bernoulli Effect, the low pressure drew the liquid solution into the atomizer where it entered the gas stream as a thin filament and further decomposed into suspended liquid droplets composed of liquid n-heptane and solid particles. As shown in Figure 6, the spray stream and droplets were directed towards

an impaction surface where the larger droplets impacted the surface and entered the reservoir bottle (waste). Since the smaller droplets s had lower momentum, they avoided the impaction surface and followed the airstream directed out of the atomizer to the appropriate experimental apparatus. The gas entering the atomizer, atomizer pressure, and solution were varied depending on the experiment.

Most pneumatic atomizers can be configured in two modes: recirculation and non-recirculation mode. Recirculation mode is utilized when the solvent has low volatility. In recirculation mode, the solution is drawn into the atomizer from a reservoir bottle. After the solution is atomized, excess liquid is drained into the same reservoir bottle where it can be atomized again. Operating in recirculation mode is problematic when using a volatile solvent because the solvent gradually evaporates in the atomizer. As a result, the concentration of the solution continuously increases, and larger particles are developed with continual use. Since a volatile solvent was used in this study, the atomizer was operated in non-recirculation mode (shown in Appendix A Figure 1). The syringe pump delivered a constant flowrate of solution to the atomizer and the excess liquid was drained in a separate reservoir bottle and discarded.

2.3 Particle Instrumentation

This study characterized the produced nanoparticles using either a Scanning Mobility Particle Sizer (SMPS) or Engine Exhaust Particle Sizer (EEPS). Both the particle instruments were developed at TSI in Shoreview, MN. The SMPS was used to characterize

particles in steady state conditions while the EEPS was used to characterize particles in real time. The EEPS was used specifically for the autoignition experiments allowing detection of how the nanoparticle morphology changed as temperature increased prior to, and during autoignition.

2.3.1 SMPS

The TSI Scanning Mobility Particle Sizer (SMPS) which consists of a 3080 Electrostatic Classifier and a 3025A Condensation Particle Counter (CPC) were used in series to characterize particles based on size and number concentration. A detailed description of the electrostatic classifier and CPC can be found in TSI's operation and service manuals, and a schematic of the two instruments can be found in Appendix A Figure 2 and Appendix A Figure 3. The electrostatic classifier consists of a bipolar charger, flow controller, and a Differential Mobility Analyzer (DMA) for size classification.

A polydisperse submicrometer aerosol stream enters the classifier at a rate of 1.5 lpm and is directed towards an impactor which is used to remove large particles. The impactor works on the principal of inertia; smaller particles are able to follow the streamline and bypass the impactor, while larger particles impact the plate. Next, the aerosol passes through a Kr-85 bipolar charger that neutralizes the particles. After neutralization, the aerosol is directed towards the DMA where particles are collected based on their electrical mobility. Electrical mobility is calculated using Equation 2.5[36] where n is the number of elementary units of charge, e is the charge on the electron, C_c is the slip

correction factor, η is the gas viscosity, and d is the diameter of the particle. The resulting calculation shows that electrical mobility is indirectly proportional to particle size.

$$Z = \frac{neC_c}{3\pi\eta d} \quad \text{for Re} < 1 \qquad \textbf{(2.3)}$$

Both sheath air and the aerosol stream enter the DMA at flowrates of 15 and 1.5 lpm, respectively. The DMA is a large cylinder that contains an inner cylinder rod charged to 0 to 10,000 V depending on the size of the particle to be collected which produces an electrical field inside the DMA. Negatively charged particles will repel the inner wall and deposit onto the outer wall while positively charged particles are attracted to the negatively charged central rod. Neutrally charged particles will exit the DMA with excess air. Particles with a narrow range of electrical mobility will pass through an open slit, exit the DMA, and enter the CPC to be counted. Based on the DMA and the flow rates used for this study, the classifier is able to collect particles ranging from 6 to 230 nm.

Once the monodisperse particles leave the DMA, they enter the CPC where they are counted. Before being counted, a supersaturated vapor (butanol) condenses onto the particles and promotes growth. Next, the enlarged particles enter a laser-diode light source that optically detects the particles. The CPC is able to count particles at a concentration up to 9.99 x 10^4 particles/cm^3.

2.3.2 Engine Exhaust Particle Sizer

The engine exhaust particle sizer (EEPS) is a transient response particle instrument that is capable of measuring particles ranging from 5.6 to 562 nm by using differential

electrical mobility classification. EEPS is ideal for real time response; 10 size distributions (10 Hz) are reported each second with a step response of 1 second. The EEPS has a resolution of 16 channels per decade. A schematic of the EEPS is provided in Appendix A Figure 4.

Aerosol enters the EEPS at a flowrate of 10 lpm through a cyclone with a 1 µm cut-point. After passing the cyclone, the aerosol enters an electrical diffusion charger. First a negative charger puts a negative net charge on the particles, which helps reduce the number of charged particles that enter the second charger. Next, a predictable net positive charge is applied to the particles. The charged particles and 40 lpm of sheath air enter the top of the analyzer column where the flow is directed towards the bottom of the column. An electric field is produced inside the column by two concentric cylinders. The central rod is divided and insulated into three different voltage levels: 85, 470, and 1200 V respectively, while the outside column consists of 22 electrode rings producing various positive voltages. The various electric fields inside the analyzer repel positively charged particles outwards based on their electrical mobility; particles with high electrical mobility are directed towards the top electrode rings.

2.3.3 Dilution System

The inlet particle concentration limit for the SMPS and EEPS is 1 x 10^5 particles/cm^3 and 1x 10^7 particles/cm^3 respectively. A two-stage dilution system shown in Figure 7 was used to ensure particle concentrations stayed below the instruments' limits.

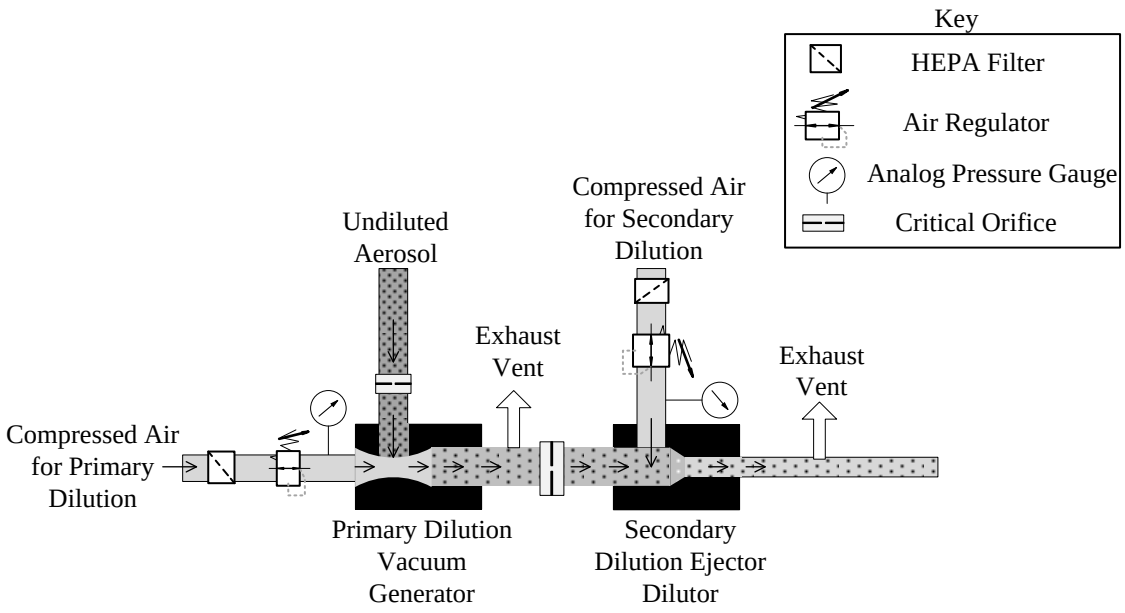

Figure 7: Dilution System used in the experimental study

The primary dilution system used an Air-VAC AVR038H Vacuum Generator with a port for filtered compressed dry air (CDA), a vacuum port, and an exhaust port. The pressurized air enters the vacuum generator through a small circular opening to generate a high velocity air stream. This pressurized air expands creating a pressure drop inside the vacuum. Due to the Bernoulli Effect, the pressure drop inside the vacuum generator draws the undiluted aerosol stream through the vacuum port where it becomes diluted with the CDA. To control the undiluted aerosol flowrate and increase the dilution ratio, a .02" critical orifice was placed upstream of the vacuum port.

The dilution ratio is calculated from the two flowrates entering the vacuum generator. The CDA flow rate was collected using a rotameter. When using a rotameter

with pressurized air, the flowrate must be corrected for pressure effects.[36] Matheson rotameters provides correction factors for various pressures. The flowrate was obtained using Equation 2.4. $Flowrate_{CAC}$ is the flowrate of the CDA, corrected for pressure (lpm). $Flowrate_{Rotameter}$ is the uncorrected flowrate shown on the rotameter (lpm).

$$Flowrate_{CAC} = Flowrate_{Rotameter} * Correction\ Factor \quad \textbf{(2.4)}$$

The undiluted aerosol flowrate was obtained via a Sensidyne Gilibrator 2 which collects flowrates between 20 cc/min to 6 LPM. The primary stage dilution is calculated using the following equation:

$$Primary\ Dilution = \frac{Flowrate_{CAC} + Flowrate_{UndilutedSample}}{Flowrate_{UndilutedSample}} \quad \textbf{(2.5)}$$

Next, the diluted aerosol was sent to the secondary dilution system. Similar to the primary dilution setup, the newly diluted aerosol first passed through a .02" critical orifice to minimize the flowrate entering the secondary dilution system. Since the flowrate leaving the primary dilution was higher than the flowrate entering the secondary dilution system, a bypass port was added thus causing most of the primary diluted sample to exit at this point. The aerosol that passed through the critical orifice then entered an Air-Vac TDSS Series ejector dilutor. An ejector dilutor is a well-established, low-cost method for diluting raw exhaust with minimal losses and good mixing.[39] The Air-VAC TDSS series is similar to a vacuum generator; however, the pressurized air flows through a small annular opening. This allows for a higher flowrate of CDA to enter the ejector thus allowing even higher dilution ratios. The flowrate of the CDA entering the secondary dilution system was

measured using a rotameter with correction for pressure. The aerosol stream entering the secondary vacuum port was collected using the flow calibrator. The secondary dilution equation is provided in Equation 2.6.

$$Secondary\ Dilution = \frac{Flowrate_{CAC,2} + Flowrate_{PrimaryDilutedSample}}{Flowrate_{PrimaryDilutedSample}} \quad \textbf{(2.6)}$$

$Flowrate_{CAC,2}$ is the flowrate corrected for pressure entering the second vacuum generator (lpm) and the $Flowrate_{PrimaryDilutedSample}$ is the flowrate of the once diluted aerosol stream entering the vacuum port on the secondary vacuum generator (lpm). The overall dilution system is obtained by multiplying the two dilution ratios:

$$Overall\ Dilution\ Ratio = Primary\ Dilution\ * Secondary\ Dilution \quad \textbf{(2.7)}$$

Dilution is beneficial because it can inhibit particle growth through mechanisms like agglomeration and coagulation.[36,40] Inhibiting agglomeration provides more accurate concentration and size measurements of the particles.

2.4 Experimental Setup

2.4.1 Particle Characterization of In-Situ generated Nanoparticles Experiment

The objective of the first experiment was to validate that the atomization process was creating suspended PCHE nanoparticles. The particles exiting the atomizer were collected and characterized by particle size and concentration. The two factors of interest were: 1) the concentration of the solution dissolved in n-heptane in weight percent (wt %) and 2) the pressure of the CDA entering the atomizer in psig. The four concentration levels

studied were: 0.00, 0.01, 0.05, and 0.10 wt %. A 0.00 wt % solution (n-heptane-no PCHE present) was tested to characterize the impurities like oils and metal particles present in the n-heptane. The second parameter, atomizer air pressure, was tested at three levels: 25, 30 and 35 psig to quantify how particle size and total concentration varied with pressure. All twelve factor-level combinations tested in this experiment are shown in Table 3's test matrix. A total of three rounds of experiments were completed to analyze repeatability, and for each round of data collected four consecutive tests were performed over all 12 factor-level combinations.

Table 3: Particle Characterization of PCHE Nanoparticles: Number of Tests Completed for each Trial

Trial #	Pressure (psig)	Solution (wt %)			
		0.00	**0.01**	**0.05**	**0.10**
1	**25**	4 Tests	4 Tests	4 Tests	4 Tests
	30	4 Tests	4 Tests	4 Tests	4 Tests
	35	4 Tests	4 Tests	4 Tests	4 Tests
2	**25**	4 Tests	4 Tests	4 Tests	4 Tests
	30	4 Tests	4 Tests	4 Tests	4 Tests
	35	4 Tests	4 Tests	4 Tests	4 Tests
3	**25**	4 Tests	4 Tests	4 Tests	4 Tests
	30	4 Tests	4 Tests	4 Tests	4 Tests
	35	4 Tests	4 Tests	4 Tests	4 Tests

A schematic of the experimental setup is shown in Figure 8.

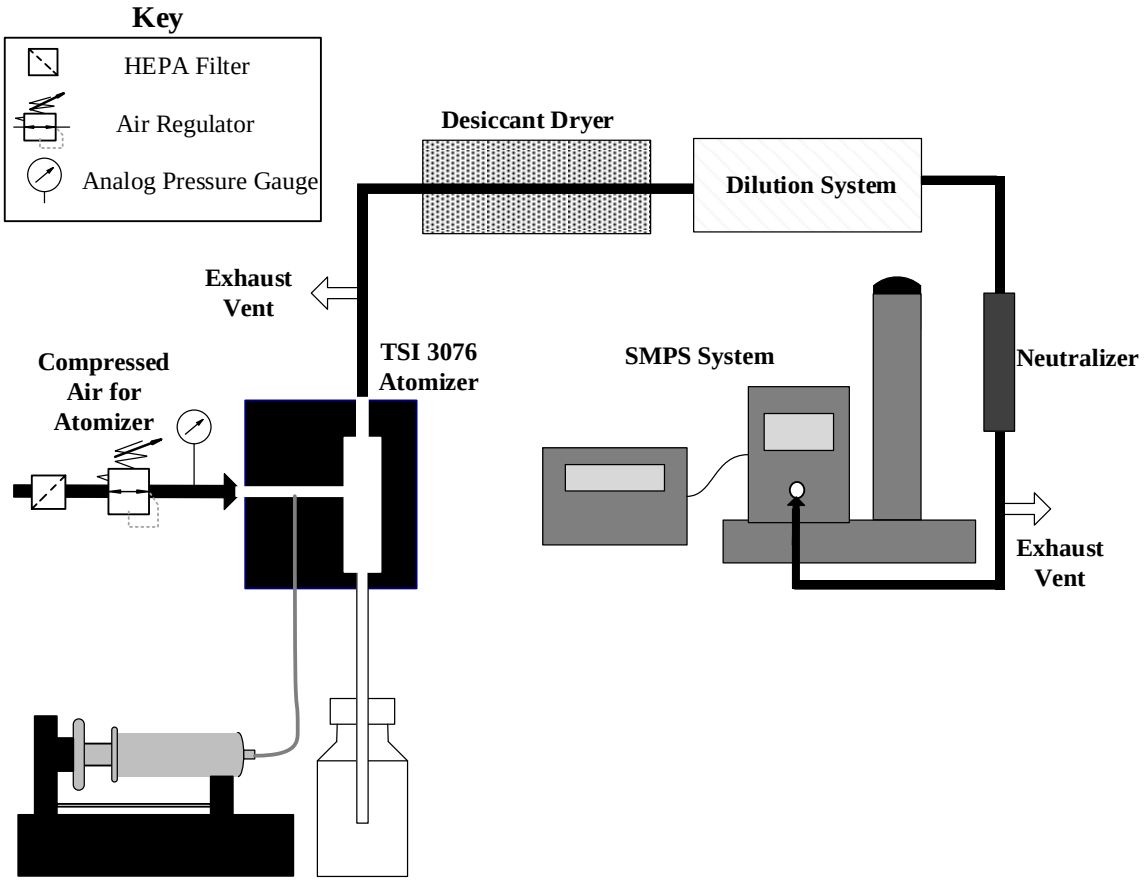

Figure 8: Particle Characterization Experimental Set-up

First, the pressure of the CDA (25, 30 or 35 psig) was set on the atomizer. The solution to be tested was collected in a 35 ml syringe and placed in the syringe pump. The pump was turned on, and solution was delivered to the atomizer to generate PCHE nanoparticles using the procedure described in Section 2.2. The aerosol was directed out of the atomizer into 1/4" silicon conductive tubing. Conductive tubing inhibits the build-up of static charge to help eliminate particle loss to the tubing wall.[41] The conductive tubing was connected to a cylindrical desiccant dryer (27" long with a diameter of 3.5") filled

with activated carbon to remove the evaporated n-heptane from the aerosol stream by adsorbing the volatile material onto the surface of the desiccant. Activated carbon was used because it is relatively cheap and has a large, porous, surface area which provides optimal adsorption capability.[42]

The particles were injected into the two-stage dilution system (described in Section 2.3.3) to decrease the particle concentration below the SMPS's limits. The primary and secondary dilutions were set to 60 and 40 (psig), respectively for all tests in Table 3. As mentioned previously, the primary stage's vacuum generator controlled the flowrate into the dilution system. Since the aerosol flowrate exiting the desiccant was greater than the incoming flowrate controlled by the dilution system, a bypass port was placed before the dilution system to allow excess flow to exit the system.

Due to the high dielectric constant of the solution, the liquid droplets produced inside the atomizer experienced electrolytic charging as they separated from the atomizer surface. Consequently, the generated aerosol developed a high electrostatic charge exiting the atomizer; particles with high electrostatic charge are more likely to adhere to tube walls and other surfaces.[36] To minimize particle loss, a neutralizer was placed downstream of the dilution system where the aerosol was neutralized to the Boltzmann charge equilibrium.

After the particles were neutralized, they were directed towards the SMPS and particle size and concentration measurements were collected. The SMPS collected data for 135 seconds for particles ranging from 5.94 to 224.7 nm. After the SMPS was done

scanning, the data collection for one test was complete, and the pump was manually disabled. To avoid cross-contamination, n-heptane was atomized between tests with different solution concentrations, and the syringe was replaced to clean the system and remove any residual particles. Contamination within the setup was checked between tests by collecting data using the SMPS with only CDA (no solution entering the system).

The experiment was repeated using the organic compound Dioctyl sebacate (DOS) instead of PCHE. DOS is miscible in n-heptane; therefore, the PCHE results were compared to the DOS results to confirm that PCHE was miscible in n-heptane. DOS is a liquid at room temperature and is often used with isopropanol to check the consistency of the SMPS and EEPS for particle number concentration and aerosol size distribution.[43] It is known that 100 ppm of DOS diluted in isopropanol produces an aerosol with a geometric mean diameter ranging between 50-60 nm.[43] The test matrix for DOS is shown in Table 4.

Table 4: Particle Characterization of DOS Nanoparticles: Number of Tests Completed for each Trial

Trial #	Pressure (psig)	Solution (weight %)			
		0.00	0.01	0.05	0.10
1	25	4	4	4	4
	30	4	4	4	4
	35	4	4	4	4
2	25	4	4	4	4
	30	4	4	4	4
	35	4	4	4	4
3	25	4	4	3	4
	30	4	4	4	4
	35	4	4	4	4

2.4.2 Thermal Degradation Experiment

The objective of the second experiment was to quantify the thermal degradation temperature of PCHE nanoparticles in a laminar flow reactor (LFR) based on a similar study conducted by Shimizu *et al*.[44] A LFR is a type of chemical reactor that controls the reaction rate by using laminar flow and a constant temperature surrounding the reactor.[45] Operating the LFR in the laminar flow regime ($236 \leq Re \leq 568$) results in a velocity profile that is inherently two-dimensional and parabolic, thus creating a radial temperature gradient inside the reactor. Likewise, a finite time is needed to equilibrate the gas flow with the reactor's wall temperature which creates a distinct temperature gradient inside the reactor.[44]

This study used a LFR made of quartz tube (1.9 cm OD, 1.4 cm ID, and 50.8 cm in length) that was heated using a Lindberg Blue Mini-Mite programmable Tube Furnace.

The furnace is 41 cm wide, but the heated section inside the furnace is only 30.5 cm in length. The specifications for the furnace are provided in Appendix A Table 1. The furnace temperature was collected from a Type- K thermocouple manufactured inside the furnace near the electrical heating coils. The quartz tube was connected to the system with Swagelok Ultra Torr vacuum fittings used with high temperature Kalrez O-rings (rated for 315 ˚C). The length of the quartz tube was longer than the furnace, so the Swagelok fittings and O-rings wouldn't be exposed to temperatures past their limit.

There were two parameters of interest in the second experiment: 1) the concentration of the solution dissolved in n-heptane and 2) the temperature inside the furnace. The two solutions studied were the 0.00 and 0.10 wt % of PCHE dissolved in n-heptane. The 0.00 wt % solution was used as the base solution to quantify the degradation of the impurities so it could be differentiated from the degradation of the PCHE nanoparticles. When polymers start to thermally degrade, polymer chains break causing a decrease in the molecular weight. A good indication of polymer degradation is a shift in particle size.

The test matrix for the thermal degradation experiment is provided in Table 5 and indicates how many tests were completed at each factor level combination. Three rounds of data were collected.

Table 5: Thermal Degradation Test Matrix for PCHE

Trial #	Solution (wt %)	Furnace Temperature (˚C)										
		25	**75**	**150**	**200**	**250**	**300**	**400**	**500**	**600**	**700**	**800**
1	**0.00**	2	2	2	2	2	2	2	2	2	2	2
	0.10	2	2	2	2	2	2	2	2	2	2	2
2	**0.00**	3	3	3	4	3	3	3	3	3	3	3
	0.10	3	3	3	3	3	3	3	3	3	3	3
3	**0.00**	2	0	0	0	2	0	2	2	2	2	2
	0.10	2	0	0	0	2	0	2	2	2	2	2

A schematic of the experimental setup is shown below in Figure 9.

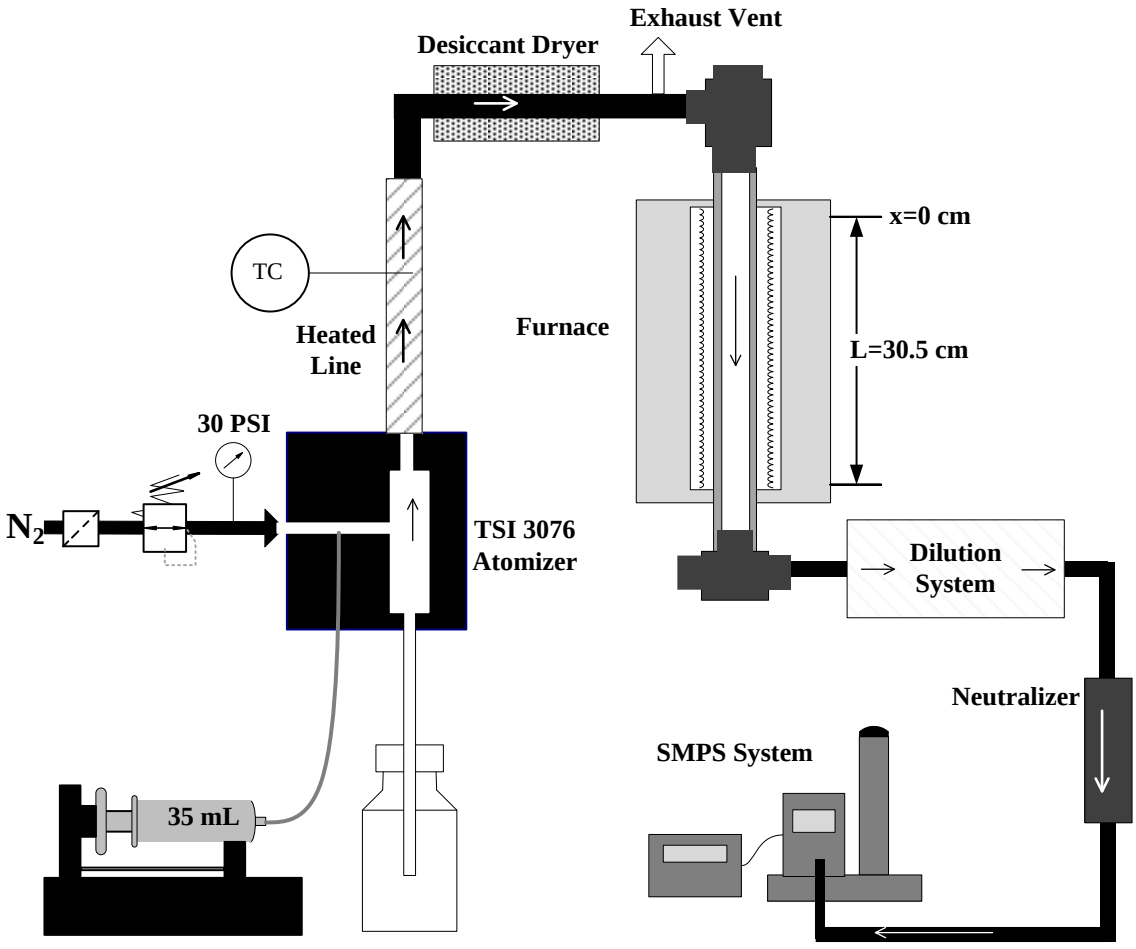

Figure 9: Thermal Degradation Experimental Set-up

The PCHE nanoparticles were developed with the TSI 3076 atomizer using the same procedure in Section 2.2. Nitrogen gas (N_2) atomized the solution at a fixed pressure of 30 psig. Using an inert gas like N_2 inhibits the fuel mixture from combusting in the laminar flow reactor (combustion requires fuel and an oxidant). Using an inert gas like N_2 was necessary because a portion of the n-heptane vapors entered the LFR due to the desiccant dryer not being 100% efficient. In addition, the N_2 gas inhibited the oil impurities

from forming smoke (oil has a smoke point of approximately 200 ˚C in the presence of an oxidant).

Before starting a test, the furnace was set to a desired temperature, while, the N_2 gas and primary and secondary dilution CDA were set to pressures of 30, 57, and 38 psig, respectively. Turning on the compressed gases allowed for a constant flow rate to circulate through the reactor. The flowrate through the reactor and dilution system was controlled by the vacuum generator in the primary dilution system. Since the flowrate exiting the desiccant was greater than the flowrate generated by the primary dilution system, a bypass port was placed downstream of the desiccant dryer. The flowrate through the reactor was created by the vacuum generator in the primary dilution system. Once the desired furnace temperature was steady for approximately five minutes, data was ready to be collected via the SMPS using the procedure mentioned below.

First the solution of interest was atomized, and the aerosol stream was directed out of the atomizer through stainless steel tubing (24" long and ½" OD). The tubing was surrounded by heat tape and insulation, which was used to heat the aerosol stream inside the tubing to 50 ˚C. The elevated temperatures promoted vaporization of the liquid n-heptane droplets in the aerosol stream to increase the concentration of n-heptane collected on the desiccant (desiccant can only capture volatile vapors).[46] An Omega type K thermocouple was installed inside the tubing to collect the aerosol temperature and heating tape was controlled by a temperature controller. Next, the aerosol passed through the

desiccant dryer to capture the n-heptane. After passing through the desiccant dryer, the aerosol was directed to the LFR where the particles were heated. Finally, the aerosol exited the flow reactor and passed through the dilution system, neutralizer, and SMPS, sequentially.

After initial data analysis, a more detailed sweep of the 0.10 wt % solution was collected between the furnace temperatures of 600-800 ˚C using the same procedure described in the prior paragraph. The test matrix for the sweep is shown below in Table 6.***Table 1***

Table 6: Furnace Sweep of the 0.10 wt % PCHE Solution

Trial #	Furnace Temperature (˚C)								
	600	**625**	**650**	**675**	**700**	**725**	**750**	**775**	**800**
1	2	2	2	2	2	2	2	2	2
2	3	2	2	2	2	2	2	2	2

The temperature of the furnace did not represent the temperature profile inside the laminar plug flow reactor. The aerosol stream was exposed to a finite heating rate with the laminar flow condition which created a distinct temperature gradient inside the reactor.[44] To understand the axial centerline's temperature profile inside the reactor at various furnace conditions, two Omega Type-K thermocouples were placed inside the reactor as shown in Figure 10. The furnace was then set, and once the temperature was steady, temperature readings from the two thermocouples were collected at 1 Hz inside the reactor. The thermocouples were positioned in various locations inside the plug flow reactor to

obtain a total of five temperature readings. The thermocouple data were collected using a NI SCXI-1000 Chassis and LabVIEW software.

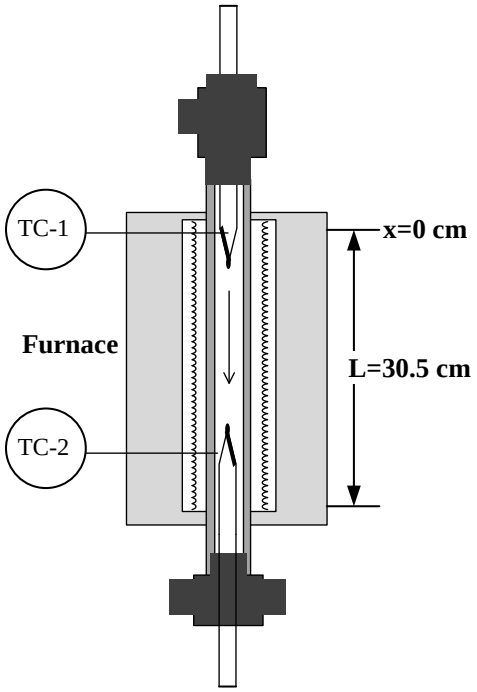

Figure 10: Furnace with Thermocouples Placed Inside Reactor

2.4.3 Autoignition Temperature Experiment

During the third experiment, the autoignition temperature of the PCHE and n-heptane solutions was determined by sending a reactive mixture through the laminar flow reactor. The solutions were atomized using filtered, CDA at a pressure of 30 psig. Five different solutions were tested in this study: iso-octane and PCHE dissolved in n-heptane at four concentrations (0.00, 0.01, 0.05, and 0.10 wt %). Since the autoignition characteristics of n-heptane and iso-octane are well established, iso-octane was included in

the autoignition experiments to compare the autoignition characteristics of the two surrogate fuels. The furnace was programmed to create a temperature ramp inside the laminar flow reactor as shown below in Figure 11. First, the temperature was set to 100 ˚C for five minutes. After five minutes, the temperature increased 50 ˚C every minute until the temperature reached 650 ˚C and 750 ˚C for the n-heptane and iso-octane solutions, respectively. Autoignition temperature was collected by a thermocouple placed at the outlet of the LFR and data was recorded with a NI DAQ and LabVIEW software.

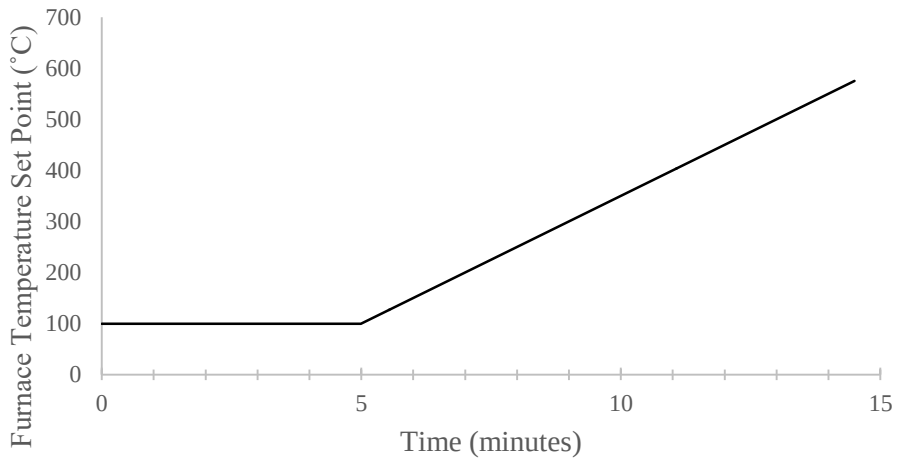

Figure 11: An example of the temperature ramp used for the n-heptane solutions during the Autoignition Temperature Experiments

An additional thermocouple was placed outside of the laminar flow reactor to collect the temperature of the furnace during the experiment. A schematic of the setup is shown in Figure 12.

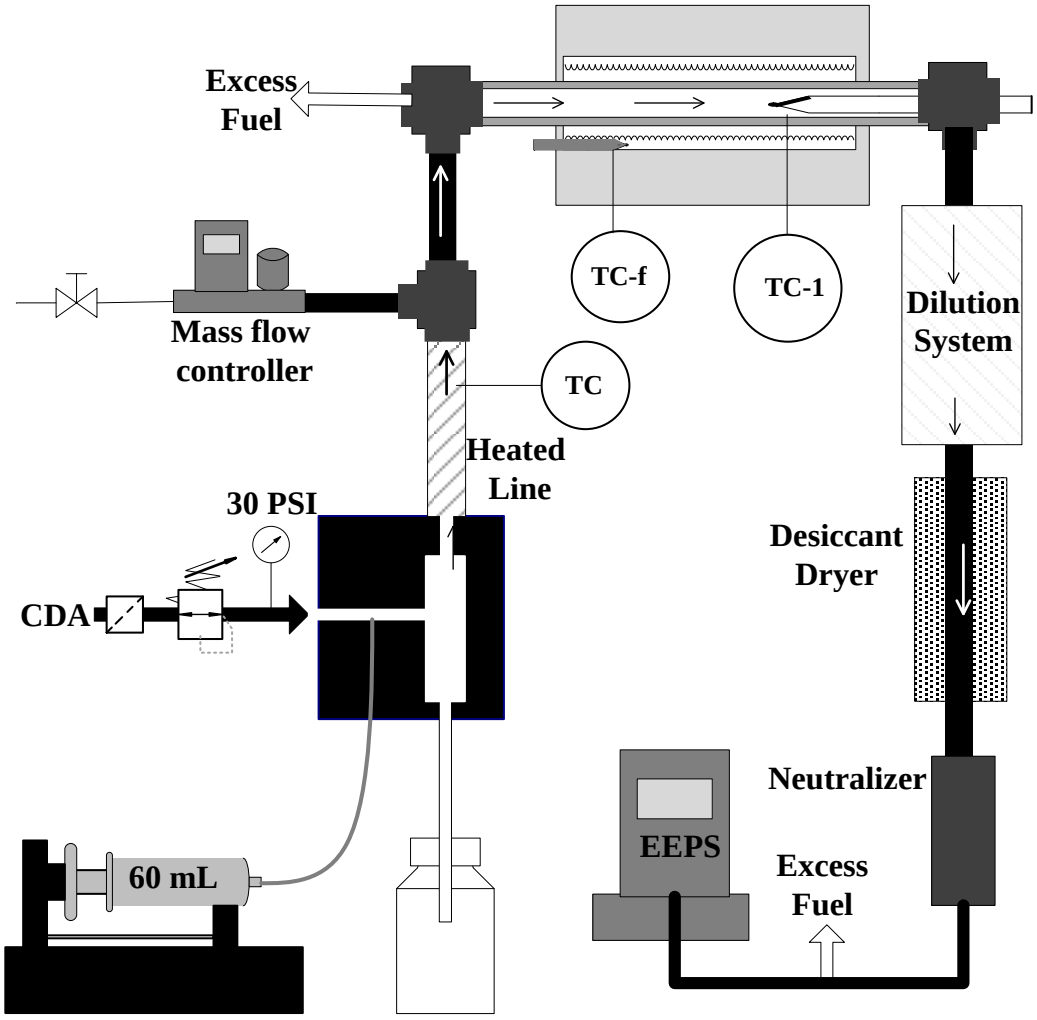

Figure 12: Reactor Experimental Set up

A line supplying CDA was added to the system downstream of the atomizer to dilute the atomized aerosol. The flow rate of the CDA was controlled by an Alicat Scientific Mass Flow controller and was set to 5 lpm. Dilution was necessary to obtain a fuel-air ratio within n-heptane's flammability limits. An exhaust vent was placed upstream of the laminar flow reactor to control the flowrates in the system. The flowrate entering the

reactor was controlled by the dilution system pressures and was around 1.40 lpm. A Technical Glass Products porous quartz frit (14 cm OD and 2.5 mm thickness) was placed at the inlet of the plug flow reactor as a safety device to prevent flashback into the atomizer and compressed air lines.

Before beginning each test, the furnace temperature was set to 100 ˚C. The mass flow controller was turned on, and the atomizer, the primary dilution and secondary dilution pressures were set to 30, ~60, and ~40 psig, respectively to provide a dilution ratio of roughly 315. The dilution system pressures were adjusted until an acceptable flow rate of around 1.40 lpm entering the dilution system was obtained. After the furnace was steady at 100 ˚C, data was ready to be collected using the procedure mentioned below.

The solution was atomized at 30 psig using CDA. Next, the flowrate would enter the heated stainless steel tube set to 50 ˚C. The aerosol would then enter the laminar flow reactor where it would be heated followed by the desiccant dryer where the unburned n-heptane would be captured. The aerosol stream was directed to the dilution system, neutralizer, and EEPS, sequentially to collect real time response of particle characterization.

2.5 Experimental Analysis

2.5.1 Particle Analysis

All three experiments collected particle data either using the SMPS or the EEPS instruments. The raw concentration collected by the particle instruments was corrected for each test by multiplying by the corresponding dilution ratio. When multiple sets of data

were collected for each parameter, statistical analysis was performed to analyze the results. Analysis included calculating the average $\bar{x}_r$ and standard deviation, σ_r, for each round, r, of data. Individual data sets were examined, and outliers were removed using ASME's Thompson Outlier Criteria[47] shown in Equation 2.8. Thompson's outlier criteria, τ_r, is dependent on the data set's standard deviation and sample size. For an individual data point, x, to be considered an outlier, it must be greater than the product of the standard deviation and the outlier criteria.

$$x > \tau_r \sigma_r \tag{2.8}$$

The overall average for the entire experiment, $\bar{X}$, was calculated by averaging the means ($\bar{x}_r$) for the three rounds of data.

$$\bar{X} = \frac{\bar{x}_1 + \bar{x}_2 + \bar{x}_3}{3} \tag{2.9}$$

The overall error was calculated accounting for accuracy and precision. Accuracy error, u_a, accounts for the error associated between data points within a particular round.

$$u_a = \frac{2\sigma_1 + 2\sigma_2 + 2\sigma_3}{3} \tag{2.10}$$

Precision error, u_p, accounts for the error between the rounds of data:

$$u_p = 2 * \sqrt{\left({}^1\!/_3 \sum_{r=1}^{3} (\bar{x}_r - \bar{X})^2 \right)} \tag{2.11}$$

The total error, u_{Total}, is calculated using Equation 2.12.

$$u_{Total} = \sqrt{(u_a)^2 + \left(u_p\right)^2} \quad \textbf{(2.12)}$$

The SMPS collected a total of 102 particle sizes and corresponding concentrations for diameters ranging from 5.94 to 224.7 nm. Particles were numbered with the increment n; n=1 represents the smallest particle collected and increases by one until the largest particle is accounted for (n=102).

The particle concentration data collected in the first experiment was converted to a volume distribution by using Equation 2.13. The volume distribution, VD_n, represents the volume of particles normalized by particle size for particles ranging from d_n to d_{n+1}. Volume distributions help visualize where the majority of the total particle mass comes from in a distribution.[48]

$$VD_n = \frac{dV_n}{dDp * Vt} \quad \textbf{(2.13)}$$

In Equation 2.13, (dDp) represents the size range of the particles, which is calculated using Equation 2.14.

$$dDp = d_{n+1} - d_n \quad \textbf{(2.14)}$$

The change in volume, dV_n, for the size interval was calculated assuming a perfect sphere using the mean diameter in the size interval. C_n represents the concentration of particles at diameter d_n.

$$dV_n = \left[\frac{(d_{n+1} + d_n)}{2}\right]^3 * \frac{\pi}{6} * C_n \quad \textbf{(2.15)}$$

The total volume, Vt, was calculated by summing all the individual change in volumes.

$$Vt = \sum_{n=1}^{n=102} dV_n \quad \textbf{(2.16)}$$

The particle distributions obtained during the *Autoignition Temperature Experiments* were collected in real time using the EEPS and were divided into three sections based on reactions that occurred in the laminar flow reactor: before low temperature heat release (LTHR), between LTHR and high temperature heat release (HTHR), and after HTHR. The total concentrations for selected particle distributions in each of the three sections were calculated.

2.5.2 Residence Time Analysis

The aerosol's residence time through the reactor was calculated in the *Thermal Degradatio*n and *Autoignition Temperature* Experiments. As shown in Equation 2.17, the residence time is given by:

$$t = \frac{V}{Q} \quad \textbf{(2.17)}$$

Where V is the volume of the flow reactor, and Q is the flowrate of the aerosol through the reactor. The reactor was cylindrical with a radius of r and a length of L. In this study, L represents the length of the heated section inside the furnace which was 30.5 cm. As such, V can be represented by:

$$V = \pi r^2 L \quad \textbf{(2.18)}$$

2.5.3 Reynold's Number Analysis

Assumptions regarding the velocity and temperature profile inside the LFR were made based on the LFR operating in the laminar flow regime ($236 \leq Re \leq 568$). To ensure a laminar profile through the reactor, the Reynold's number was calculated for the *Thermal Degradation* and *Autoignition Temperature Experiment*s using Equation 2.19:

$$Re = \frac{4\rho Q}{\pi D \mu} \tag{2.19}$$

2.5.4 Equivalence Ratio Analysis

To ensure the fuel would combust during the *Autoignition Experiment*, the equivalence ratio was calculated at various fuel and air flow rates. The equivalence ratio, ϕ, is the fraction of the actual fuel-air ratio to the stoichiometric fuel-air ratio.[7]

$$\phi = \frac{\frac{F}{A}}{\left(\frac{F}{A}\right)_s} \tag{2.20}$$

In the presence of an oxidant and fuel source, a fuel will only ignite if the fuel concentration corresponding to the equivalence ratio is within the flammability limit. The lower flammability limit (LFL) is the lowest concentration of fuel (in the presence of oxygen and a heat source) that will ignite. Similarly, the upper flammability limit (UFL) is the highest concentration of fuel that will ignite in the presence of an oxygen and heat source. It should be noted that the flammability limits vary with pressure and temperature. Outside the flammability limit, the mixture will not ignite.[7,49]

The fuel-air ratio is calculated on a mass (or mass flowrate) basis using the following equation:

$$\frac{F}{A} = \frac{m_f}{m_a} = \frac{\dot{m}_f}{\dot{m}_a} \qquad \textbf{(2.21)}$$

The stoichiometric fuel-air ratio for n-heptane was calculated using the procedure mentioned below (refer to *Appendix B: Iso-octane Equivalence Ratio Calculations* for the iso-octane fuel-air ratio equations). First, the number of moles in the stoichiometric combustion equation were found using Equation 2.22:

$$C_7H_{16} + 11(O_2 + 3.76N_2) \rightarrow 7CO_2 + 8H_2O + 11 * 3.76N_2 \qquad \textbf{(2.22)}$$

In the stoichiometric equation, there is 1 mole of fuel and 52.36 moles of air. The moles were multiplied by the corresponding molecular weight to obtain the stoichiometric mass of the fuel and air.

$$\left(\frac{F}{A}\right)_s = \left(\frac{m_f}{m_a}\right)_s = \frac{n_f * MW_{fuel}}{n_a * MW_{air}} = \frac{1\ mol * 100.21\ g/mol}{52.36\ mol * 28.97\ g/mol} = .06605 \qquad \textbf{(2.23)}$$

Next, the actual fuel-air ratio was obtained using the procedure mentioned in the following paragraph. The *Autoignition Experiment* only used atomizer pressures of 30 psig; thus, the fuel-air ratios were only calculated at this pressure. In the experiments, it was assumed that the polymer additive did not alter the stoichiometric fuel air ratio of a given fuel. Therefore, only the equivalence ratio for n-heptane and iso-octane were calculated.

The fuel mass flow rate was calculated using the following procedure. First, the reservoir bottle for excess fuel was emptied and weighed using a scale. Next, the reservoir

bottle was connected back to the atomizer, the atomizer pressure was set to 30 psig, and the n-heptane was atomized at a fuel flowrate of 2 ml/min for a total of five minutes. After five minutes, the mass of the excess fuel was measured using the scale. The fuel mass flow rate exiting the atomizer into the reactor was calculated using Equation 2.24.

$$\dot{m}_f = \dot{m}_{syringe} - \dot{m}_{excess} \quad \textbf{(2.24)}$$

For the *Autoignition Experiment*, $\dot{m}_{syringe}$ was set to 2 ml/min for all tests, and $\dot{m}_{excess}$ was the mass of the fuel in the reservoir bottle divided by 5 minutes.

Air was introduced into the system through the atomizer ($\dot{V}_{atomizer}$) and mass flow controller ($\dot{V}_{MFC}$) which was set to 5 ml/min. The air flowrate exiting the atomizer was measured using a Gillian Gillibrator. The air flow rate through the reactor was the sum of the two air flowrates:

$$\dot{V}_a = \dot{V}_{atomizer} + \dot{V}_{MFC} \quad \textbf{(2.25)}$$

The air mass flowrate was calculated by multiplying by the density of air, ρ (1.225 kg/m^3):

$$\dot{m}_a = \dot{V}_a * \rho \quad \textbf{(2.26)}$$

2.5.5 LTHR and HTHR Analysis

In this work, the autoignition of n-heptane with and without the PCHE additive at different additive mass concentrations was studied. Autoignition was detected in the laminar flow reactor by determining the temperature where the fuel and air mixture begin to react by examining the heat released from the reaction. Heat release is the amount of

heat released from an exothermic reaction. The fuel's molecular structure will dictate the chemical kinetics (heat release rates) during ignition. Most straight chain alkanes, like n-heptane, exhibit LTHR followed by HTHR during ignition.[50] LTHR is common in straight chain alkanes because they produce intermediate radical species at relatively low temperatures which causes reaction rates to increase and oxidation to occur.[51] However, branched-chain alkanes, like iso-octane, are not as reactive at low temperatures because less intermediate species are formed, thus LTHR generally only occurs at higher pressure.[52] HTHR is the rapid oxidation of hydrocarbons that occurs when the fuel is exposed to elevated temperatures and pressures. Most of the fuel's chemical energy is expended during the HTHR portion of the heat release.

The heat release profiles were studied in the plug flow reactor by calculating the outlet temperature gradient. Temperature data was collected inside the reactor using an Omega Type K thermocouple at the outlet of the reactor (placed 40 cm from the left hand side of the plug flow reactor) as shown in Figure 13.

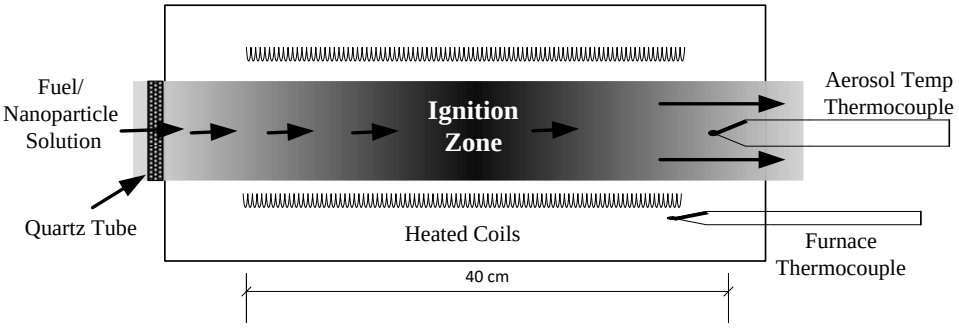

Figure 13: Thermocouple placement inside Furnace for Autoignition Experiments

The NI DAQ and LabVIEW software collected temperature readings at 2 Hz, and the temperature gradient, $\frac{dT_i}{dt_i}$, was calculated for each point by using Equation 2.27 where T_i represents the outlet temperature at time t_i.

$$\frac{dT_i}{dt_i} = \frac{T_i - T_{i-1}}{t_i - t_{i-1}} \tag{2.27}$$

LTHR and HTHR occur when the reactor temperature rapidly increases with respect to time. To analyze the rapid increases in the temperature gradient, the percent change for the temperature gradient was calculated:

$$\%\Delta\frac{dT}{dt} = \frac{\frac{dT_i}{dt_i} - \frac{dT_{i-1}}{dt_{i-1}}}{\frac{dT_{i-1}}{dt_{i-1}}} \tag{2.28}$$

In Equation 2.28, large values of $\%\Delta\frac{dT}{dt}$ represent a spike in the temperature, which is an indication of heat release. For this study, the temperature at which heat release occurred was based on preliminary data collected with the LFR which showed visual spikes in the temperature plots at the temperature gradients shown below.

LTHR Requirements: $200°C \geq Ti \geq 350°C \; and \; \frac{dT_i}{dt_i} > 2\frac{°C}{s} \quad and \quad \%\Delta\frac{dT}{dt} > 75\%$

For each trial, the first temperature that met the LTHR requirement was considered the LTHR temperature.

HTHR Requirements: $Ti \geq 450°C \quad and \quad \frac{dT_i}{dt_i} > 3\frac{°C}{s} \quad and \quad \%\Delta\frac{dT}{dt} > 40\,\%$

Similar to the LTHR requirements, the first temperature that met the HTHR requirements was considered the HTHR temperature.

3 Results and Discussion

3.1 Particle Characterization of In-Situ Generated Nanoparticles Results

The objective of the first experiment was to create a laboratory bench setup that mimics fuel droplet evaporation in a SI engine using pneumatic atomization. Particles exiting the atomizer were collected with a SMPS to analyze the particle size and concentrations confirming the atomization process produced suspended PCHE nanoparticles. In addition, the atomizer pressure and concentration of the solution were varied to quantify how the two factors altered particle characteristics.

Validating that the Atomization Process Produced Solid PCHE Nanoparticles

Figure 14 shows the average particle distributions from three rounds of repeated experiments. The y-axis represents the particle number concentration normalized by the size range of the particles (dN/dlogDp) while the x-axis represents the particle diameter, Dp. First, a 99.9% pure n-heptane solution was tested at all three atomizer pressures to determine a baseline reading. One can infer from the n-heptane curves that other particles besides the PCHE additive were present since no n-heptane particles are expected due to its high volatility. These particles were likely impurities such as oils or metal particles.

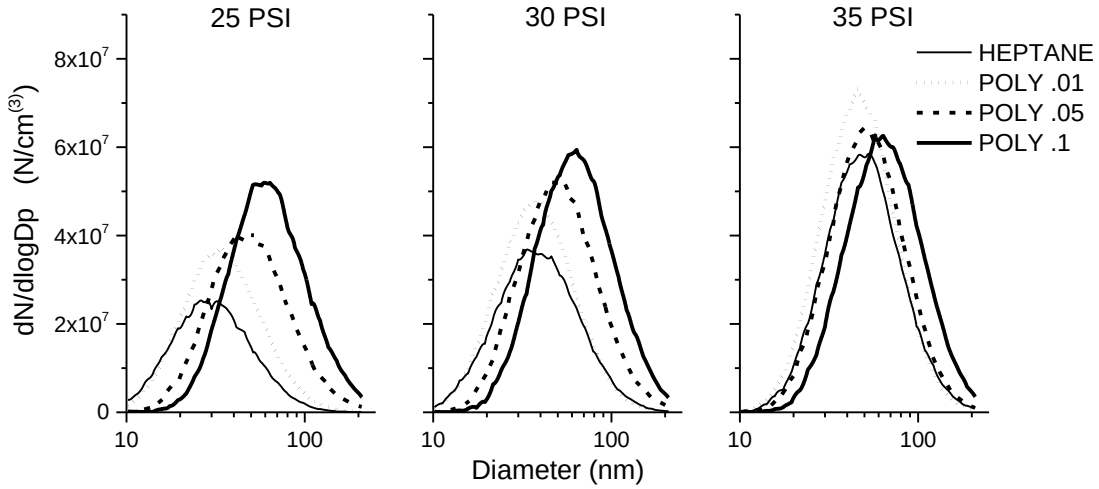

Figure 14: Particle concentrations at the three atomizer pressures using n-heptane and three polymer fuel concentrations (0.01, 0,05 and 0.1 wt %)

Next, the solutions with varying concentrations of PCHE were compared to the base solution (n-heptane). As shown in Figure 14, the shift in the normal distributions towards greater particle size and concentration confirms that the PCHE was present in the formed particles. In addition, the plots infer that the macro-sized PCHE crystals dissolved in the n-heptane. If the PCHE was insoluble in n-heptane, the PCHE crystals would have remained macroscopic sized when placed in the n-heptane solution. However, the shift in particle size with PCHE present infers the PCHE dissolved into individual polymer chains. As a result, the n-heptane droplets contained individual polymer chains and impurities that coalesced to form agglomerates as the droplet evaporated.

The plots in Figure 14 also show that the PCHE polymer chains formed agglomerates with the impurities. If the impurities did not agglomerate during the

atomization process, then a bimodal distribution would have been present with one mode representing the impurities and another mode representing the PCHE nanoparticles. Instead, the particles grew in size, indicating that the PCHE chains combined with the impurities to form agglomerated particles.

To validate PCHE's solubility in n-heptane, the results were compared to DOS (Figure 15) since it is known that DOS is soluble in n-heptane. With DOS being an oil and PCHE a solid particle, the results differed slightly. However, the overall trends between the DOS and PCHE distributions were similar indicating that PCHE is similarly soluble in n-heptane.

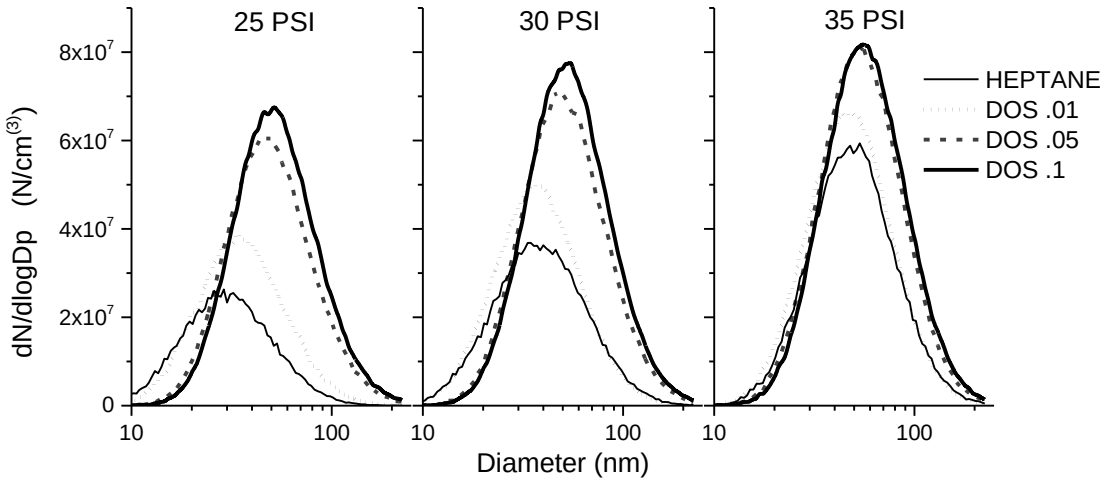

Figure 15: Particle concentrations at the three atomizer pressures using n-heptane and three DOS concentrations (0.01, 0,05 and 0.1 wt %)

The polymer solutions were added on a weight percent basis. Thus it was expected that the total mass of the system would increase as the solution concentration since

increased since volume is equal to mass times effective density. To validate this assumption, the total volume of the particles were calculated for the twelve factor level combinations (Figure 16).

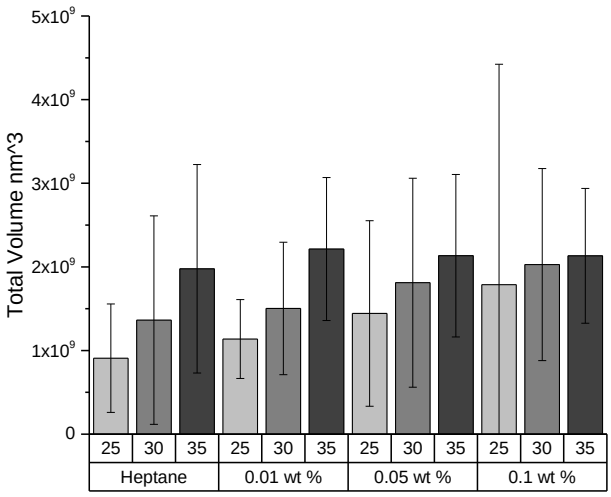

Figure 16: Total Volume for the four PCHE/n-heptane solutions (0.00, 0.01, 0,05 and 0.1 wt %)

Figure 16 shows when the atomizer pressure was held constant, the total particle volume increased as the solution concentration increased. This indicates that the total particle mass produced through spray drying increased as the solution concentration increased, confirming that PCHE particles were present. It should be noted that the error bars on the column chart are very large because the total volume calculation was dependent on the total

particle concentration, had large variance (Refer to Figure 18). The size of the error bars is discussed in the next section.

Effects of Varying Solution Concentration

As mentioned previously, smaller particles have larger specific surface area, which can increase adsorption capabilities; therefore, smaller particles were desired for this study. After verifying that the atomization process was able to produce solid nanoparticles composed of impurities and PCHE polymer chains, the next step in the experimental work was to understand how the particle size and concentration varied with atomizer pressure (i.e. solvent droplet size) and solution concentration.

As shown in Equation 1.10, it was found that particle size is directly proportional to droplet diameter and solution concentration; for this study, it was assumed that the droplet diameter remained constant within each trial. The relationship between particle size and solution concentration is shown in Figure 17. It was assumed that the concentration of impurities remained constant for each test; therefore, the increase in particle size was attributed to the number of polymer chains per droplet increasing as the weight percent of the solution increased. As an effect, the overall particle size increased during droplet evaporation. The largest increase in particle size was at 25 psig between n-heptane and the 0.10 wt% solution. The geometric mean particle diameter increased from 29.9 nm for the n-heptane solution to 62.2 nm at the 0.10 wt% solution, an increase of 107%. There was no significant increase between the 0.00 and 0.01 wt % solution at all three atomizer

pressures. Therefore, the generated nanoparticles primarily consisted of impurities when the PCHE concentration was low.

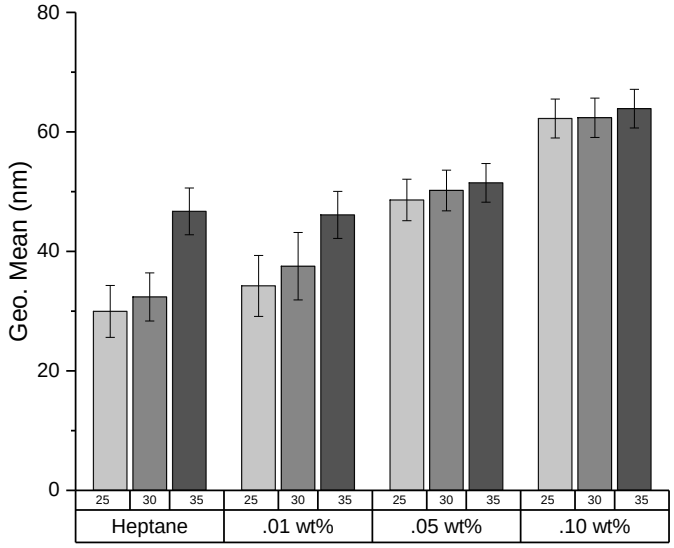

Figure 17: Geometric mean particle diameter for each factor-level combination for the four PCHE/n-heptane solutions

Next, the total number concentration of particles produced with respect to solution concentration was studied (while keeping atomizer pressure constant). The total number concentrations for the twelve factor level combinations are shown above in Figure 18. At 25 and 30 psig, the total particle concentration of particles increased as the weight percent of the solution increased. At both pressures, the total concentration of particles increased by approximately 80% for the 0.10 wt% solution compared to the solution with only n-heptane. At 35 psig, the total concentration of particles was lower for the n-heptane solution,

but the particle concentration at the 0.01, 0.05, and 0.10 wt% solution all were around 3.5E7 particles.

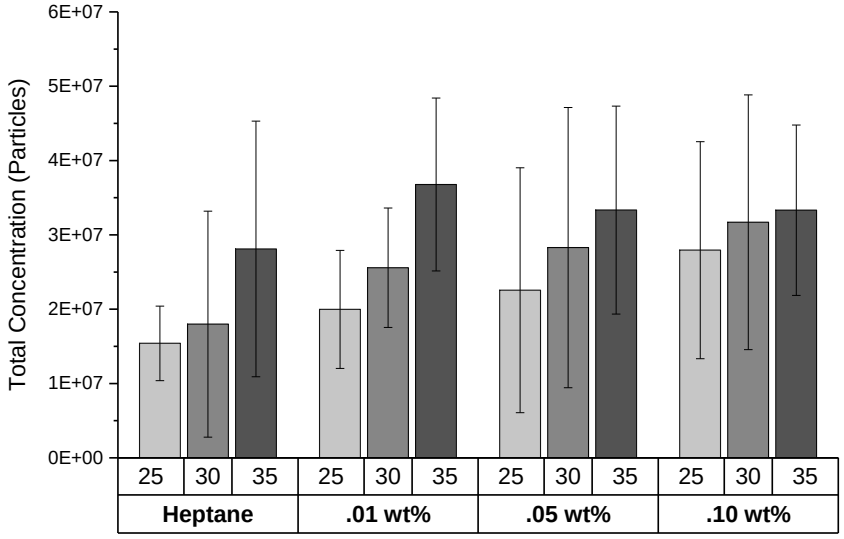

Figure 18: Total Concentration of solid particles for the four PCHE/n-heptane solutions (0.00, 0.01, 0,05 and 0.1 wt %)

The large error seen in Figure 18 stems from uncertainty arising when correcting the concentrations for the dilution ratio factor. Although the dilution system pressures were unaltered between the rounds of data in the *Particle Characterization Experiment*, the flowrates entering the dilution system varied considerably, thus changing the dilution ratio in between the three rounds of tests. Unfortunately the dilution ratios were only checked at the end of each round of data collected; therefore, the dilution ratios shown in Table 7 do not accurately represent the actual dilution ratio experienced for each rounds' individual trials. It was found that over time the PCHE particles started to clog the orifices used to

control dilution. In future experiments, the dilution system should be cleaned and the flowrates should be collected between each trial.

Table 7: Dilution Ratio Correction Factor for the Three Rounds of Data Collected in the *Particle Characterization Experiments*

Round	DR
1	319
2	311
3	315

Effects of Varying Atomizer Pressure

Next, the effects of atomizer pressure were considered while keeping the additive concentration constant. As shown in Figure 17, the particle size only increased at low solution concentrations (0.00 and 0.01 wt %) when the pressure increased to 35 psig. Otherwise, the particle size had no noticeable increase with increasing atomizer pressure and constant solution concentration. Conversely, atomizer pressure had a major impact on total concentration of particles formed. The general trend in Figure 18 shows that atomizer pressure was directly proportional to total concentration of particles present. During atomization, the gas applies a shear force, which breaks up the liquid solution into tiny droplets. It is likely that high pressures caused a larger shear force, thus promoting formation of smaller droplets that exited the atomizer without hitting the impaction plate (due to their small size). Although it is unclear why the particles grew when the atomizer pressure was at 35 psig for the 0.00 and 0.01 wt % solutions, one possible reason is that

agglomeration occurred downstream of the atomizer exit, thus causing an increase in particle size.

For all trials, particle loss was likely inside the system due to particles depositing on fittings or being captured on the activated carbon desiccant. Although such systemic errors in particle measurement existed that may preclude accurate quantitative estimation of particle number, it reasonable to assume that the error for each trial was approximately equal since dilution ratios, line lengths and temperatures remained constant throughout the experiments.

The hypothesis of this study was that a high particle surface area may promote gas phase radical scavenging. Greater number of smaller particles is more desired for this purpose because of their large specific surface area compared to fewer, larger diameter particles. Although the 0.01 wt % solution had the smallest particles, there was an insignificant difference in polymer size between the 0.00 and 0.01 wt % solution. This indicated that the particle concentration was too low, and the particles mostly consisted of impurities that would not inhibit the autoignition of n-heptane. It is also likely that the polymer and impurities combined to create mixed composition particles without the desired functionality of PCHE nanoparticles alone. However, at the 0.05 and 0.10 wt % solutions there was a significant increase in particle size compared to the base solution, thus a significant amount of PCHE polymer chains were present in each nanoparticle. For example, at 30 psig, the geometric mean diameter for the n-heptane solution was 30 nm

while the 0.05 and 0.10 wt % solutions' diameters were approximately 50 and 62 nm, respectively. Although the atomizer pressure did not change the particle size at the 0.05 and 0.10 wt % solutions, it did increase the total concentration of particles. Based on the assumption that higher particle concentrations would increase the overall radical scavenging during autoignition, higher atomizer pressures would be more likely to participate in radical scavenging. Therefore, an atomizer pressure of 30 psig was chosen for the thermal degradation and autoignition experiments.

3.2 Thermal Degradation

In order for the PCHE nanoparticles to participate in radical scavenging which is important for reducing knock, they must have high thermal stability to ensure that thermal decomposition does not occur before autoignition. To test PCHE's thermal stability, degradation temperatures were collected inside the LFR using a nitrogen atmosphere. The *Particle Characterization Experiment* proved that impurities were present in the n-heptane; therefore the 0.00 wt % solution was analyzed during the *Thermal Degradation Experiment* to understand how the n-heptane impurities degraded. The results were compared to the 0.10 wt % solution to differentiate solid impurities from the PCHE nanoparticles. It was also determined in the *Particle Characterization Experiment* that the particle concentration was highly sensitive to the flowrates in each trial; therefore, the three rounds of data were analyzed separately and the trends in the data were compared. Table 8 highlights the flowrates entering the LFR, residence time, and Reynold's number at 25 ˚C for each trial.

The Reynold's number likely fluctuated inside the LFR because of its temperature dependency, but for simplicity, it was only calculated assuming a temperature of 25 ˚C. Table 8 shows that the flow entering the LFR was operating in the laminar flow regime for all *Thermal Degradation Experiments*.

Table 8: Reynold's Number and Residence Time Calculations for the Thermal Degradation Experiments

Trial #	Solution (wt %)	Reynold's # at 25 ˚C	Residence Time (s)
1	0.00	291	1.06
	0.10	291	1.06
2	0.00	294	1.05
	0.10	288	1.08
3	0.00	300	1.03
	0.10	286	1.08

Analyzing the Temperature Profile Inside the LFR

Before analyzing thermal degradation of the PCHE nanoparticles, the axial centerline temperature profile inside the LFR at various furnace temperature set points was collected at a residence time of approximately 1.06 seconds. Figure 19 provides a plot of the temperatures collected and the best fit line for each.

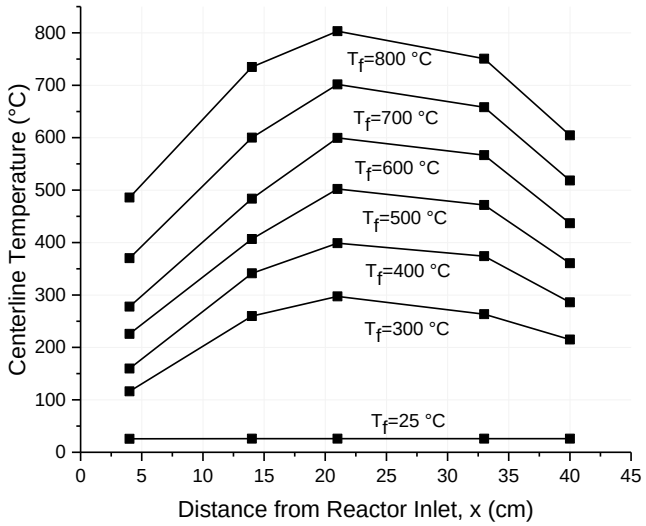

Figure 19: Axial Centerline Temperatures Inside the Reactor at Various Oven Temperature Set Points

Under the laminar flow condition, the flow inside the reactor was expected to have a parabolic velocity profile. Figure 19 proves that there was a delay in temperature rise due to the finite heating rate under the laminar flow condition. The maximum centerline temperature did not quite reach the furnace temperature set point because of the cooling towards the end of the reactor. The variable temperature profile inside the laminar flow reactor makes it difficult to understand the exact thermal degradation temperature in the LFR. To simplify the results, the data was analyzed qualitatively based on the furnace temperature set points.

Thermal Degradation of n-heptane Impurities

Figure 20 shows the normalized particle concentration for n-heptane (without additive) distributions with error bars (gray shadowing). In each of the three plots below, the particle distribution varied with temperature indicating that the nanoparticles at the reactor outlet changed as a function of furnace temperature.

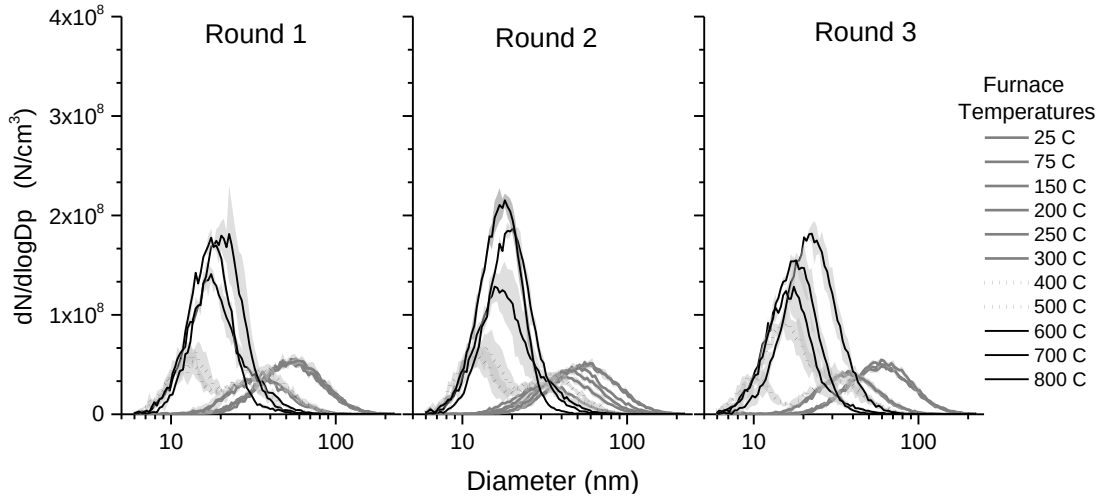

Figure 20: Particle Distribution Plots for n-heptane (no additive) with the Furnace Temperature Set Point Spanning from 25-800 ˚C

In all three rounds, there were three distinct distribution modes present. Modes were divided by furnace set point temperatures that had approximately the same particle distributions. To clearly visualize the three distribution modes, the Round 2 data from Figure 20 was divided into the three modes and is shown in Figure 21.

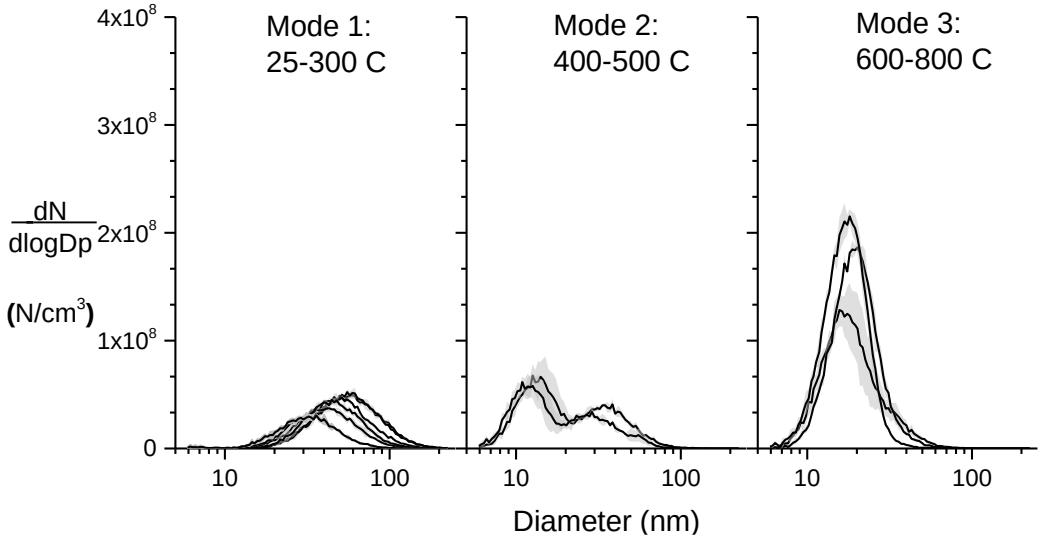

Figure 21: n-Heptane's Particle Distribution plots divided into the three modes (2nd Round of Thermal Degradation Data Collected)

The furnace temperature set points in Mode 1 spanned from 25-300 ˚C. The distributions in Mode 1 were normal with a mean diameter of roughly 35 nm, similar to what was obtained in the *Particle Characterization Experiments* at 30 psi for n-heptane. In Mode 1, the impurities did not thermally degrade. In addition, the agglomerates stayed intact.

Mode 2 provides distributions for furnace set point temperatures at 400 and 500 ˚C. The distributions in Mode 2 were bimodal rather than normal. The first peak was around 15 nm while the second peak was at 30 nm. Since metal impurities have a mean diameter around 20 nm, the first peak in the distribution represented individual metal impurities while the second peak likely represented the agglomerates of the impurities. In Mode 3,

there was a sharp increase in smaller particles. Most likely, any oil impurities evaporated around a furnace temperature set point of 600 ˚C. Meanwhile, the elevated temperature likely caused agglomerates to break apart considering agglomerates are loosely held together by weak electromagnetic forces, van der Waals forces, or by interlocking; therefore, little energy was required to break the agglomerates apart[53]. As a result, mostly individual metal impurities exited the LFR in Mode 3.

Thermal Degradation of 0.10 wt % PCHE/n-heptane Solution

Figure 22 provides the three rounds of data collected for the 0.10 wt % solution of PCHE dissolved in n-heptane. Similar to the n-heptane alone, temperature affected the particle distributions, and there were also three distinct distribution modes present. Peak concentrations were higher than n-heptane alone, and the distributions were shifted to the right, indicating that PCHE nanoparticles were present.

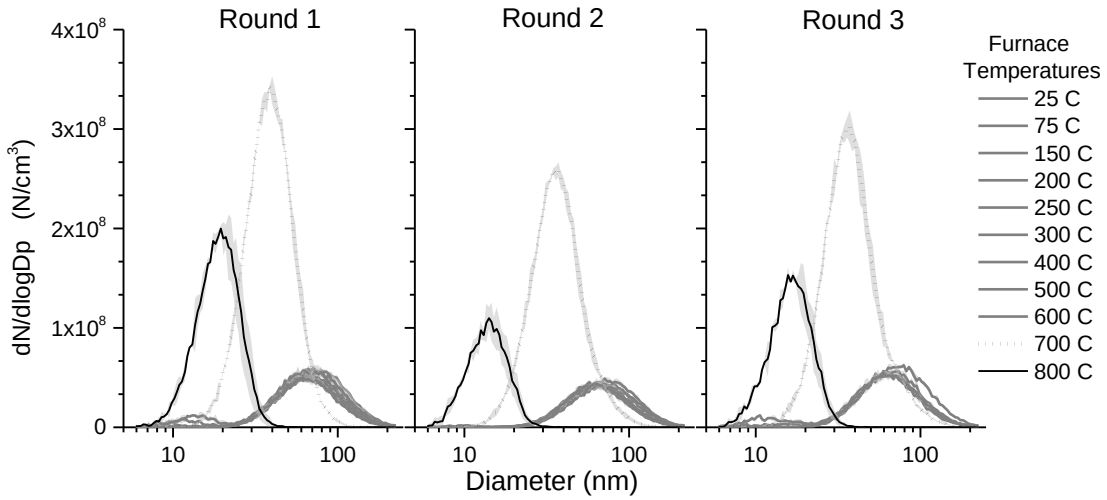

Figure 22: Particle Distribution Plots for 0.10 wt% PCHE solution with the Furnace Temperature Set Point Spanning from 25-800 ˚C

The data from Round 2 in Figure 22 was divided into the three modes as shown in Figure 23. The three modes for the 0.10 wt % solution span different temperature ranges compared to the n-heptane distributions. In Mode 1, the particle distributions were approximately the same for oven set point temperatures ranging from 25-600 ˚C. This indicated that the PCHE nanoparticles remained intact during Mode 1 indicating the agglomerates did not separate.

At 700 ˚C which constitutes Mode 2, the particle concentration spiked, and the overall particle diameter decreased to about 40 nm; this phenomenon was likely caused by separation of the PCHE agglomerates and the evaporation of the oil impurities. It is unclear whether the PCHE particles started to degrade at 700 ˚C. At 800 ˚C, the overall particle concentration and size decreased with a mean diameter around 20 nm. The drastic size and

concentration decrease indicates that the PCHE particles degraded and were so small they were no longer being detected by the SMPS. The remaining particles were likely just the metal impurities in the fuel.

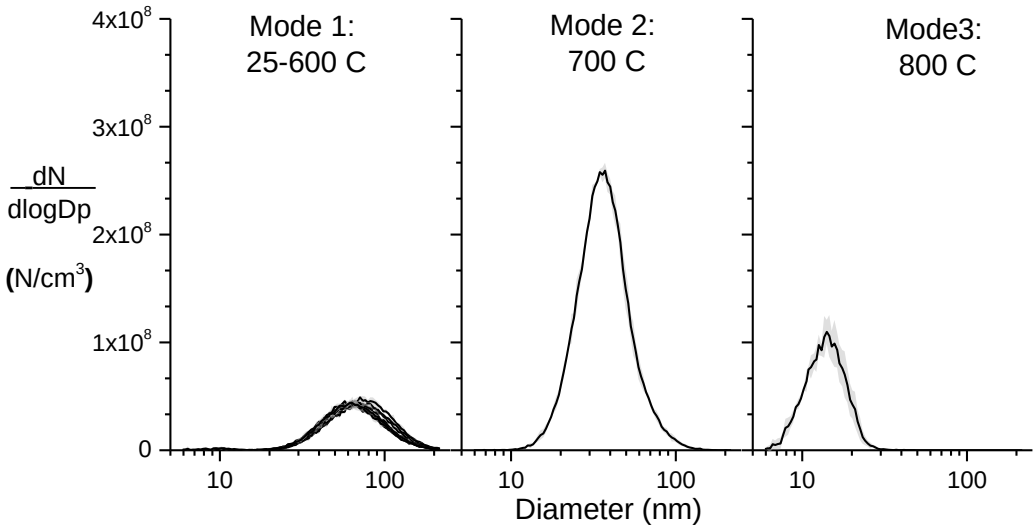

Figure 23: The 0.10 wt % solution's Particle Distribution plots divided into the three modes (2nd Round of Thermal Degradation Data Collected)

600-800 ˚C Furnace Sweep for the 0.10 wt % Polymer Solution

To further understand PCHE's degradation in the laminar flow reactor, a more thorough temperature sweep was performed with the 0.10 wt % solution for temperature

set points spanning between 600 and 800 ˚C. The residence time are provided below in Table 9.

Table 9 Reynold's Number and Residence Time Calculations for the Thermal Degradation Sweep

Trial #	Solution (wt %)	Residence Time (s)
1	0.10	1.08
2	0.10	1.14
3	0.10	1.08

The particle distributions from the Round 2 Sweep are shown below in Figure 24; all three rounds of data can be found in *Appendix C: Additional Graphs.* Again, three different distribution modes were present. In the first mode, which spans from a furnace temperature set point from 600-675 ˚C, the distributions were bimodal. Most likely, the metal impurities started to separate from the PCHE particles, which is why the first peak in the bimodal distribution was around 15 nm while the second peak was around 60 nm. In Mode 1, as the temperature rose, the number of agglomerates separating increased. This is evident as the first peak in the bimodal distribution became larger as the temperature increased. In Mode 2, which spans from 700-775 ˚C, agglomerates have completely separated and only individual particles were present. In Mode 3, particle pyrolysis occurred and the polymer degraded, and only the metal impurities and some of the broken polymer chains were present.

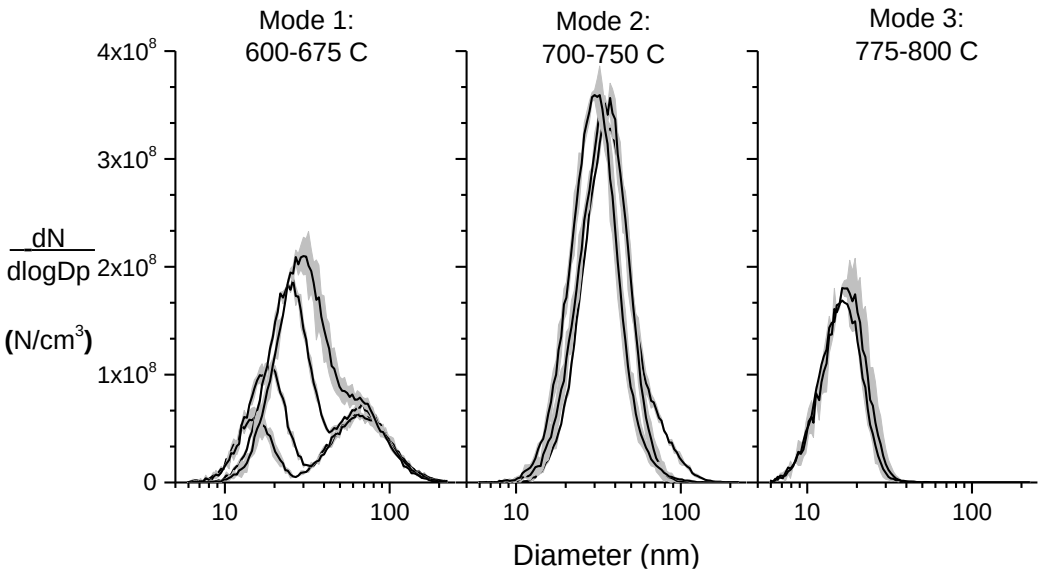

Figure 24: Particle Distributions divided into three modes for the Round 2 Thermal Degradation Sweep

It is likely that thermophoretic losses occurred in the system as the heated aerosol exited the LFR into the room temperature setup. Thermophoresis is a phenomenon in which particles suspended in a gas, subjected to a temperature gradient, migrate from the hot to the cold zones of the gas and deposit on the walls of the cold surface.[54] The larger the temperature gradient, the more likely losses are. Therefore, trials conducted at 800 ˚C likely lost more particles due to thermophoresis than trials conducted at 100 ˚C.

The results found that the agglomerates present in the nanoparticles completely separated at 700 ˚C, but the thermal degradation did not occur until 775 ˚C. Therefore, the particles should be able to participate in radical scavenging (assuming the hypothesis is true) if the autoignition temperature is below 775 ˚C. As mentioned previously, all the *Thermal Degradation Experiments* were conducted in a nitrogen gas atmosphere. This was

necessary to prevent the oils from smoking and to avoid autoignition from the n-heptane that was not captured by the desiccant dryer. Most likely, thermal degradation would happen at lower temperatures in the presence of air because oxygen can participate in radical formation reactions that accelerate the degradation of the polymer backbone.

3.3 Autoignition Experiments

The third experiment analyzed the autoignition characteristics of the 0.00, 0.01, 0.05, and 0.10 wt % PCHE/n-heptane solutions' LTHR and HTHR profiles because the heat release profile is a good indicator of a fuel's autoignition characteristics. The fuel and air flowrates were held constant for each A*utoignition Experiment* and are shown below in Table 10. Iso-octane was included in this study to check the credibility of the LFR and to ensure results matched with previous data. The approximate flammability limits for n-heptane and iso-octane are $0.6 \leq \phi \leq 4$, thus the experiments operated within the flammability limit.

Table 10: Flow rates and Equivalence Ratio for the Autoignition Experiments

Solution	**$(F/A)_s$**	**$\dot{m}_f$ (g/s)**	**$\dot{m}_{air}$ (g/s)**	**$(F/A)_{actual}$**	ϕ
n-heptane	0.0660	0.448	9.4	0.0475	0.720
Iso-octane	0.0664	0.45193	9.4	0.0479	0.722

The LTHR and HTHR temperatures were calculated by analyzing the outlet temperatures gradient. Figure 25 shows plots from four different trials: air, n-heptane, iso-octane, and a 0.10 wt % solution of PCHE dissolved in n-heptane (the 0.01 and 0.05 wt %

followed same trend as the 0.10 wt % solution). The spikes in the figure below correspond to either LTHR or HTHR.

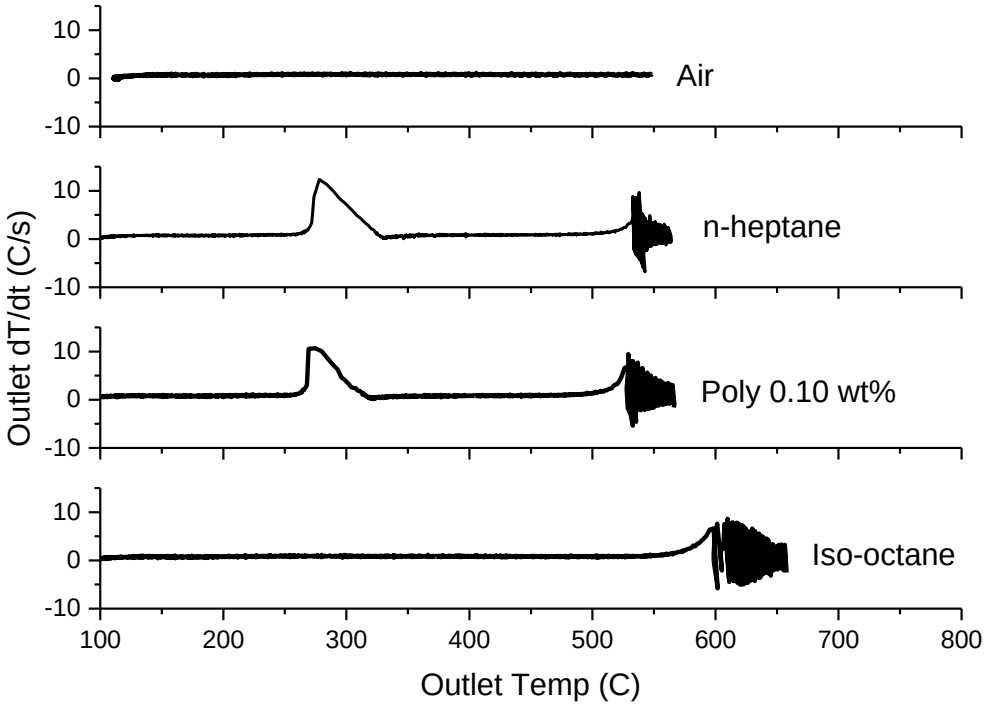

Figure 25: dT/dt versus Outlet Temperature for four Autoignition Trials

As expected, air did not experience a spike in the temperature gradient since no combustion (LTHR and HTHR) occurred. Both the n-heptane and the polymer experienced a spike in the temperature gradient near 300 and 550 ˚C corresponding to LTHR and HTHR, respectively. Iso-octane only experienced a HTHR around 600 ˚C. The two surrogate fuels, n-heptane and iso-octane's results matched with previous studies conducted by A. Ciajolo et. al.[52] The study found that n-heptane experienced both LTHR and HTHR while iso-

octane was unreactive at relatively low pressures and temperatures in a jet-stirred flow reactor. Figure 25 also shows that iso-octane's HTHR occurred at a higher temperature than n-heptane's HTHR, which was expected because iso-octane is less reactive than n-heptane, which is indicated by the higher octane number (100 RON).

The average LTHR and HTHR for the four solutions: 0.00, 0.01, 0.05, and 0.10 wt % of PCHE dissolved in n-heptane are represented in Figure 26. As shown below, the LTHR and HTHR at all four solutions were very similar. This indicates that the PCHE was unreactive during the autoignition process.

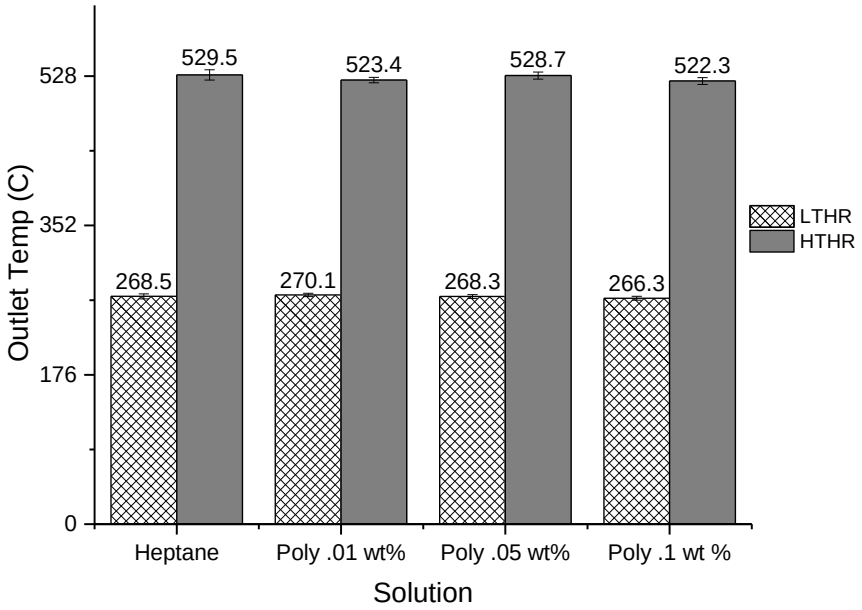

Figure 26: Average Outlet Temperatures at LTHR and HTHR

Although autoignition temperatures were not altered with the PCHE additive, the particle concentration was analyzed to detect any variation between the solutions. Figure

27 shows the particle concentration with respect to time for four different sets of data collected during the experiment (one for each of the four solutions).

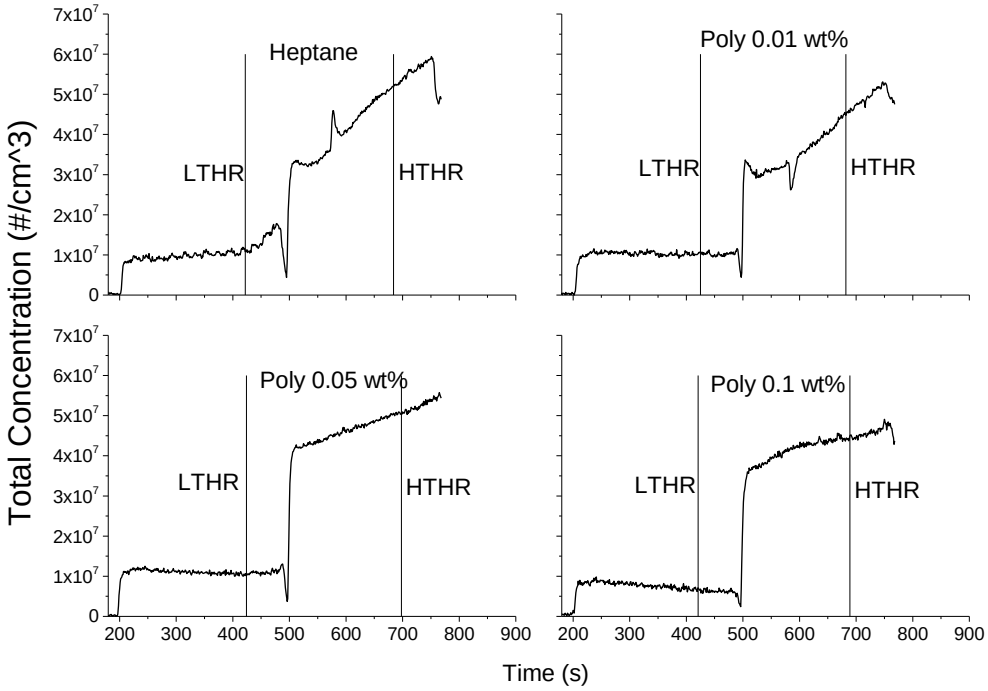

Figure 27: Total Concentration vs. Time for Four Autoignition Experiment Trials

As shown in the plots above, total particle concentration varied throughout the experiment. The n-heptane plot shows a slight increase in particle concentration after LTHR. However, this was not evident in the plots with PCHE present. In all four plots, there was a sharp spike about 100 seconds after LTHR. During this spike, the particle concentration drastically decreased followed by a drastic increase in particle concentration. Subsequently, the particles gradually increased even after HTHR. The plots do not indicate a drastic change in particle concentration at HTHR.

The increase in particle concentration was likely caused by chemical reactions between the fuel and air in the LFR. As reactions occurred, solid particles like soot were produced. It should be noted that the EEPS was not able to differentiate soot particles from the PCHE nanoparticles. Overall, it is unclear if the particles participated at all during the combustion process.

There are multiple theories why the polymer did not increase the autoignition temperature of n-heptane. First, when the PCHE polymers were generated during the atomization process, their specific surface area may have been too low limiting its ability to adsorb radicals. It is also possible that the PCHE used in this study did not have high enough adsorption selectivity to radicals like HO_2, causing it to be unreactive during the combustion process. There is also a possibility that the polymer thermally degraded before autoignition occurred. The *Thermal Degradation Experiments* occurred in a nitrogen atmosphere, but the *Autoignition Experiments* were conducted in the presence of air; therefore, it is possible that thermal degradation occurred before autoignition.

4 Conclusion and Recommendations

This study explored the potential mechanisms by which organic PCHE nanoparticles act as fuel additives to hinder the autoignition of n-heptane. The atomization process proved that the PCHE was soluble in n-heptane and was able to produce solid nanoparticles consisting of PCHE polymer chains and solid impurities. The results from the Particle Characterization Experiment found that particle size was mostly affected by the solution concentration but particle number was mostly affected by atomizer pressure. In particular, the particles' geometric mean diameter increased as the solution concentration increased. For example, at 35 psig, the 0.00 and 0.10 wt % solutions had a geometric mean diameter of 47 and 63 nm, respectively. Similarly, the total particle concentration increased as the atomizer pressure increased.

Using the LFR with a residence time of approximately 1.06 seconds, the PCHE nanoparticles started to thermally degrade around 775 ˚C in a N_2 atmosphere. The results from the autoignition experiments showed no significant difference in autoignition temperature between the four solutions (0.00, 0.01, 0.05, and 0.10 wt % of PCHE dissolved in n-heptane). Therefore, the PCHE produced during the atomization process was unable to inhibit n-heptane's autoignition characteristics in this study, which indicted PCHE nanoparticles produced in this way would not alter the knock characteristics of fuels.

Recommendations for future work on this project include capturing the particle morphology by utilizing Transmission Electron Microscopy (TEM) imaging. TEM

imaging would quantify the size, shape and porosity of the nanoparticle generated during the atomization process. Thermogravimetric analysis should also be used to understand the particle decomposition during the *Thermal Degradation* and *Autoignition Experiments*. If an organic polymer nanoparticle is found to be successful at increasing the autoignition temperature, then the polymer nanoparticle should be analyzed at pressures and temperatures similar to what an engine experiences.

Recommendations for future work include using organic polymers with high porosity to increase the overall specific surface area of the nanoparticles. Since it may be difficult to develop porous organic nanoparticles via the atomization technique used in this study, one possible method would be produce the polymer nanoparticles separately and crosslink them. The crosslinked, porous, organic nanoparticles could then be added to the n-heptane solution and atomized to create droplets with suspended particles. Since crosslinking prevents dissolving, the nanoparticles would not dissolve and lose their shape in the n-heptane; instead they will only flow in the solution. Therefore, the properties of the nanoparticle can be quantified before starting the experiments.

The flowrates were difficult to control in this study and may have resulted in confounding and inaccurate results. Therefore, flow rates should be more precisely controlled with real-time monitoring for future studies. At a minimum, the flowrate should be checked before and after each test. It is also recommended that the n-heptane impurities are minimized by utilizing a higher purity n-heptane from Sigma Aldrich (99.99% pure

instead of the 99.90% pure n-heptane). To validate the LFR, a fuel additive, like ferrocene, with known autoignition inhibition characteristics should be tested. Lastly, the thermal degradation experiments should be repeated using air instead of a nitrogen atmosphere in the LFR.

5 References

(1) Heywood, J. B. More Sustainable Transportation : The Role of Energy Efficient Vehicle Technologies. **2008**.

(2) Niven, R. K. Ethanol in gasoline: environmental impacts and sustainability review article. *Renew. Sustain. Energy Rev.* **2005**, *9* (6), 535–555.

(3) Heywood, J. B. *Internal Combustion Engine Fundamentals*; McGraw-Hill: New York, 1988.

(4) Stone, R. *Introduction of Internal Combustion Engines*, 4th ed.; Society of Automotive Engineers, 2012.

(5) Leone, T. G.; Anderson, J. E.; Davis, R. S.; Iqbal, A.; Reese, R. A.; Shelby, M. H.; Studzinski, W. M. The Effect of Compression Ratio, Fuel Octane Rating, and Ethanol Content on Spark-Ignition Engine Efficiency. *Environ. Sci. Technol.* **2015**, *49* (18), 10778–10789.

(6) Duleep, K. G. Review to Determine the Benefits of Increasing Octane Number on Gasoline Engine Efficiency - Analys and Recommendations tasks 2-5 CM-137-11-1b Final Report. *Cordinating Res. Counc. Inc.* **2012**, No. Cm.

(7) Turns, S. R. *An introduction to combustion: concepts and applications*; 2000; Vol. 499.

(8) Li, H.; Karim, G. A. Knock in spark ignition hydrogen engines. *Int. J. Hydrogen Energy* **2004**, *29* (8), 859–865.

(9) U.S. Environmental Protection Agency. EPA and NHTSA Set Standards to Reduce Greenhouse Gases and Improve Fuel Economy for Model Years 2017-2025 Cars and Light Trucks. **2012**, No. August 2012, 1–10.

(10) Pitz, W. J.; Westbrook, C. K. Chemical kinetics of the high pressure oxidation of n-butane and its relation to engine knock. *Combust. Flame* **1986**, *63* (1–2), 113–133.

(11) Nriagu, J. O. The rise and fall of leaded gasoline. *Sci. Total Environ.* **1990**, *92*, 13–28.

(12) Kameoka, A.; Tsuchiya, K. Influence of Ferrocene on Engine and Vehicle Performance; 2006.

(13) Gibbs, L.; Anderson, B. Chevron - Motor Gasolines Technical Review. **1996**, 1–69.

(14) Leone, T. G.; Olin, E. D.; Anderson, J. E.; Jung, H. H.; Shelby, M. H.; Stein, R. A. Effects of Fuel Octane Rating and Ethanol Content on Knock, Fuel Economy, and CO2 for a Turbocharged DI Engine. *SAE Int. J. Fuels Lubr.* **2014**, *7* (1), 9–28.

(15) Demirbas, A. Competitive liquid biofuels from biomass. *Appl. Energy* **2011**, *88* (1), 17–28.

(16) Anderson, J. E.; DiCicco, D. M.; Ginder, J. M.; Kramer, U.; Leone, T. G.; Raney-Pablo, H. E.; Wallington, T. J. High octane number ethanol–gasoline blends: Quantifying the potential benefits in the United States. *Fuel* **2012**, *97*, 585–594.

(17) Cirillo, G.; Iemma, F. *Antioxidant Polymers : Synthesis, Properties, and Applications.*; Wiley, 2012.

(18) Modak, A.; Nandi, M.; Mondal, J.; Bhaumik, A. Porphyrin based porous organic polymers: novel synthetic strategy and exceptionally high CO2 adsorption capacity. *Chem. Commun.* **2012**, *48*, 248.

(19) Tozawa, T.; Jones, J. T. a; Swamy, S. I.; Jiang, S.; Adams, D. J.; Shakespeare, S.; Clowes, R.; Bradshaw, D.; Hasell, T.; Chong, S. Y.; et al. Porous organic cages. *Nat. Mater.* **2009**, *8* (12), 973–978.

(20) Ouyang, Y.; Shi, H.; Fu, R.; Wu, D. Highly monodisperse microporous polymeric and carbonaceous nanospheres with multifunctional properties. *Sci. Rep.* **2013**, *3*, 1430.

(21) Rabbani, M. G.; El-Kaderi, H. M. Template-Free Synthesis of a Highly Porous Benzimidazole-Linked Polymer for CO 2 Capture and H 2 Storage. *Chem. Mater.* **2011**, *23* (7), 1650–1653.

(22) Rao, J. P.; Geckeler, K. E. Polymer nanoparticles: Preparation techniques and size-control parameters. *Prog. Polym. Sci.* **2011**, *36* (7), 887–913.

(23) Welch, M. J.; Hawker, C. J.; Wooley, K. L. The Advantages of nanoparticles for PET. *J Nucl Med* **2009**, *50* (11), 1743–1746.

(24) *Nanomaterials: A Danger or a Promise?*; Brayner, R., Fiévet, F., Coradin, T., Eds.; Springer London: London, 2013.

(25) Lacour, S. *Emerging questions for emerging technologies: Is there a law for the nano?*; 2013.

(26) Bandyopadhyay, S.; Pallavi, P.; Anil, A. G.; Patra, A. Fabrication of porous organic polymers in the form of powder, soluble in organic solvents and nanoparticles: a unique platform for gas adsorption and efficient chemosensing. *Polym. Chem.* **2015**, *6* (20), 3775–3780.

(27) Aboulkas, A.; El harfi, K.; El Bouadili, A. Thermal degradation behaviors of polyethylene and polypropylene. Part I: Pyrolysis kinetics and mechanisms. *Energy Convers. Manag.* **2010**, *51* (7), 1363–1369.

(28) Peterson, J. D.; Vyazovkin, S.; Wight, C. A. Kinetics of the thermal and thermo-oxidative degradation of polystyrene, polyethylene and poly(propylene). *Macromol. Chem. Phys.* **2001**, *202* (6), 775–784.

(29) Murata, K.; Sato, K.; Sakata, Y. Effect of pressure on thermal degradation of polyethylene. *J. Anal. Appl. Pyrolysis* **2004**, *71* (2), 569–589.

(30) Downs, D.; Walsh, A. D.; Wheeler, R. W. A Study of the Reactions that Lead to "Knock" in the Spark-Ignition Engine. *Philos. Trans. R. Soc. London A Math. Phys. Eng. Sci.* **1951**, *243* (870).

(31) Bates, F. S.; Fredrickson, G. H.; Hucul, D.; Hahn, S. F. PCHE-based pentablock copolymers: Evolution of a new plastic. *AIChE J.* **2001**, *47* (4), 762–765.

(32) Zhao, J.; Hahn, S. F.; Hucul, D. A.; Meunier, D. M. Thermal and viscoelastic behavior of hydrogenated polystyrene. *Macromolecules* **2001**, *34* (6), 1737–1741.

(33) Gehlsen, M.; Weimann, P. Synthesis and characterization of poly

(vinylcyclohexane) derivatives. *J. Polym. …* **2003**.

(34) Lean, J. T.; Ajbani, M.; Castner, E. S.; Zheng, L.; Kiehl, C. Thermoplastic elastomer composition. US 7244783 B2, July 17, 2007.

(35) InjectorTech information for petrol engine fuel injectors http://www.injectortech.co.nz/injector-information.htm.

(36) Hinds, W. C. *Aerosol technology : properties, behavior, and measurement of airborne particles*; Wiley, 1999.

(37) Dobry, D. E.; Settell, D. M.; Baumann, J. M.; Ray, R. J.; Graham, L. J.; Beyerinck, R. A. A model-based methodology for spray-drying process development. *J. Pharm. Innov.* **2009**, *4* (3), 133–142.

(38) Ricarte, R. G.; Lodge, T. P.; Hillmyer, M. A. Detection of pharmaceutical drug crystallites in solid dispersions by transmission electron microscopy. *Mol. Pharm.* **2015**, *12* (3), 983–990.

(39) Giechaskiel, B.; Ntziachristos, L.; Samaras, Z. Effect of ejector dilutors on measurements of automotive exhaust gas aerosol size distributions. *Meas. Sci. Technol.* **2009**, *20* (4), 1–7.

(40) Liu, Q.; Chen, D. R. A programmable aerosol diluter for generating time-varied sub-micrometer particles. *Aerosol Air Qual. Res.* **2014**, *14* (7), 1838–1850.

(41) Liu, B. Y. H.; Pui, D. Y. H.; Rubow, K. L.; Szymanski, W. W. Electrostatic effects in aerosol sampling and filtration. *Ann. Occup. Hyg.* **1985**, *29* (2), 251–269.

(42) Ciccioli, P.; Cecinato, A.; Brancaleoni, E.; Frattoni, M.; Km, V. S.; Liberti, A. Use of Carbon Adsorption Traps Combined with High Resolution Gas Chromatography - Mass Spectrometry for the Analysis of Polar and Non-Polar C4-CI4 Hydrocarbons Involved in Photochemical Smog Formation. *J. High Resolut. Chromatogr.* **1992**, *15*, 75–84.

(43) Kittelson, D.; Watts, W.; Walker, A.; Twigg, M. On-Road Evaluation of an Integrated SCR and Continuously Regenerating Trap Exhaust System. **2012**.

(44) Shimizu, T.; Abid, A. D.; Poskrebyshev, G.; Wang, H.; Nabity, J.; Engel, J.; Yu, J.; Wickham, D.; Van Devener, B.; Anderson, S. L.; et al. Methane ignition catalyzed by in situ generated palladium nanoparticles. *Combust. Flame* **2010**, *157* (3), 421–435.

(45) Andersen, T. S.; Coull, J. Evaluation of Models for Tubular , Laminar Flow Reactors. **1970**, 542–553.

(46) Lenggoro, I. W.; Hata, T.; Iskandar, F.; Lunden, M. M.; Okuyama, K. An experimental and modeling investigation of particle production by spray pyrolysis using a laminar flow aerosol reactor. *J. Mater. Res.* **2000**, *5*, 733–743.

(47) Thompson, W. R. On a Criterion for the Rejection of Observations and the Distribution of the Ratio of Deviation to Sample Standard Deviation. *Ann. Math. Stat.* **1935**, *6* (4), 214–219.

(48) Scientific, H. a Guidebook To Particle Size Analysis. *Distribution* **2010**, 1–17.

(49) Zabetakis, M. G. Flammability characteristics of combustible gases and vapors. *Bur. Mines Bull.* **1965**, No. 627, 1–129.

(50) Saisirirat, P.; Foucher, F.; Chanchaona, S.; Mounaïm-Rousselle, C. Spectroscopic measurements of low-temperature heat release for homogeneous combustion compression ignition (HCCI) n-Heptane/alcohol mixture combustion. *Energy and Fuels* **2010**, *24* (10), 5404–5409.

(51) Narayanan, A. M.; Jacobs, T. J. Observed differences in low-temperature heat release and their possible effect on efficiency between petroleum diesel and soybean biodiesel operating in low-temperature combustion mode. *Energy and Fuels* **2015**, *29* (7), 4510–4521.

(52) Ciajolo, A.; D'Anna, A. Controlling steps in the low-temperature oxidation of n-heptane and iso- octane. *Combust. Flame* **1998**, *112* (4), 617–622.

(53) Particle Sciences. Particle Size Distribution and its Measurement. *Part. Sci.* **2009**, *2*, 1–2.

(54) Montassier, N.; Boulaud, D.; Renoux, A. Experimental study of thermophoretic particle deposition in laminar tube flow. *J. Aerosol Sci.* **1991**, *22* (5), 677–687.

Appendix A: Instrument Schematics and Specifications

The instrument schematics are primarily taken from the TSI user manuals.

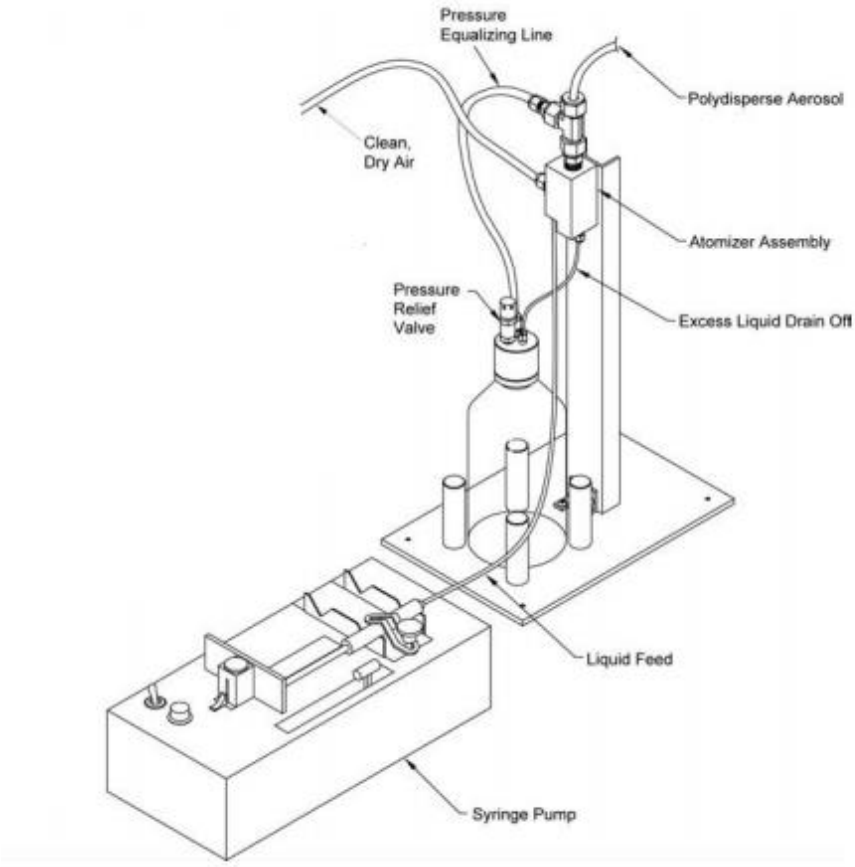

Appendix A Figure 1: Model 3076 Constant Output Atomizer set up in non-recirculation mode (Figure from TSI's Operation and Service Manual P/N 1933076)

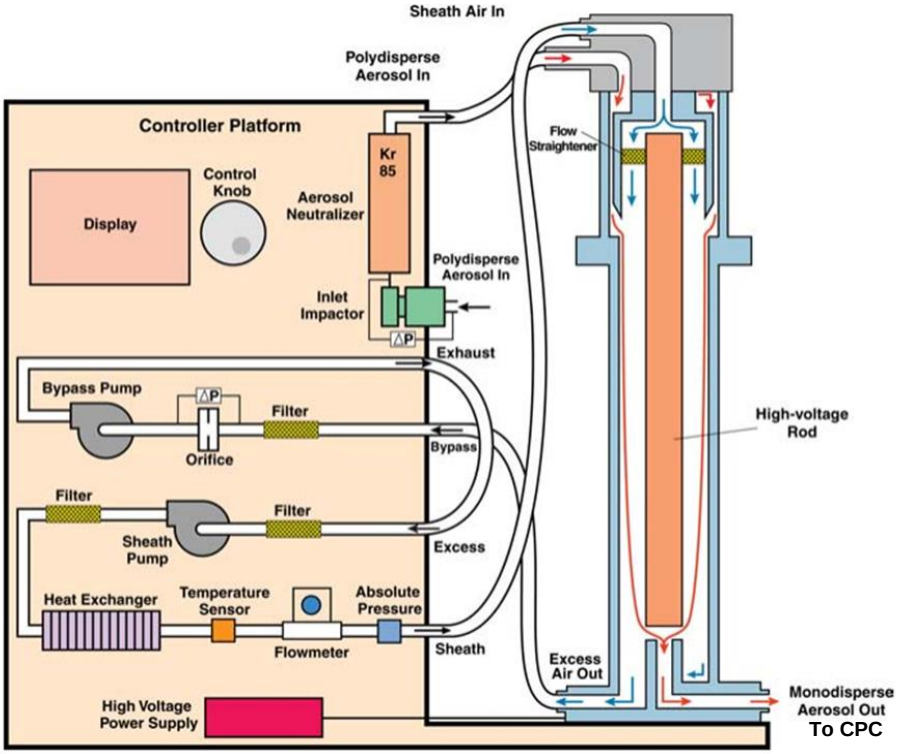

Appendix A Figure 2: Electrostatic Classifier Schematic from TSI Manual

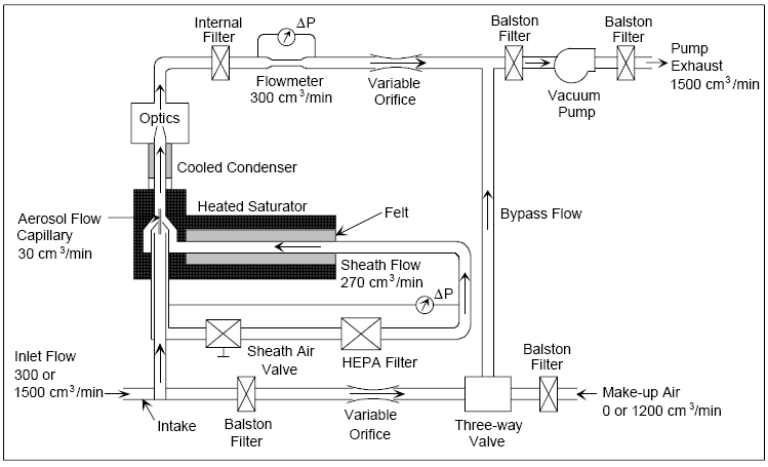

Appendix A Figure 3: Schematic of CPC from TSI Manual

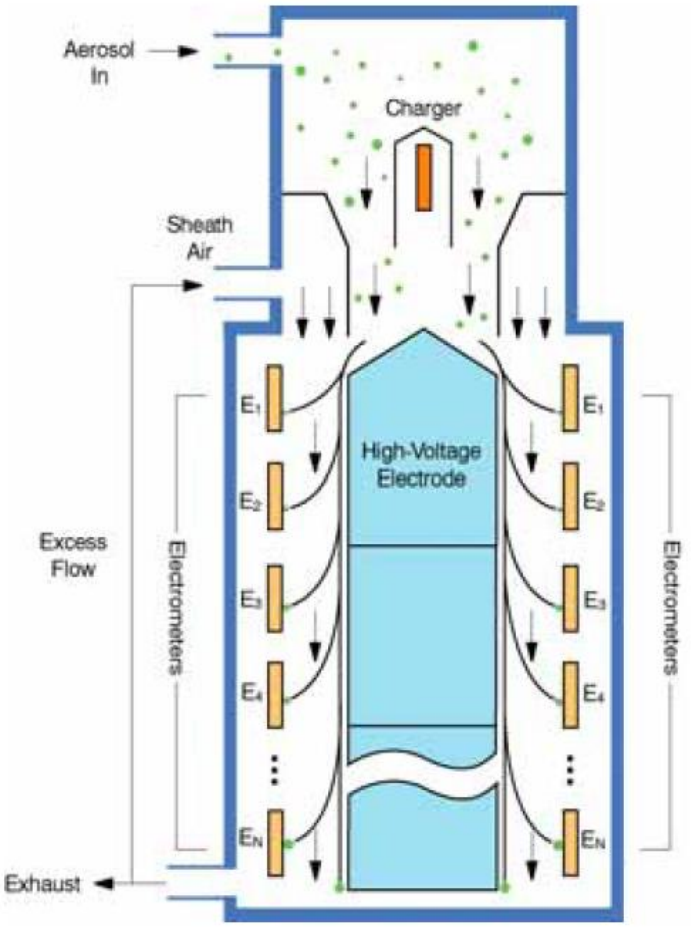

Appendix A Figure 4: Schematic of TSI's EEPS from TSI Manual

Appendix A Table 1: Lindberg Blue Mini-Mite Programmable Tube Furnace Specifications

Specifications	
Product Type	Tube Furnace
Temp uniformity	±1°C over 2-3/16" segment; ±3°C over 3-5/16" segment
Temperature range (° C) (low)	100
Heater wattage (watts)	800
Temperature range (° C) (high)	1100
Control type	16-segment
Process tube (" L)	12
Process tube (" OD)	1
Process tube (OD (mm))	25
Overall dimensions (" W)	11
Overall dimensions (" H)	15
Overall dimensions (" D)	16
Shipping weight (lbs)	37
Qty/ea	1
Brand	Thermo Scientific Lindberg
Power (VAC)	120
Power (Hz)	50/60
Manufacturer number	TF55035A-1

Appendix B: Iso-octane Equivalence Ratio Calculations

Stoichiometric Equation:

$$12.5O_2 + C_8H_{18} \rightarrow 8\,CO_2 + 9\,H_2O$$

Fuel-air ratio:

$$\left(\frac{F}{A}\right)_s = \left(\frac{m_f}{m_a}\right)_s = \frac{n_f * MW_{fuel}}{n_a * MW_{air}} = \frac{1\ mol * 114\ g/mol}{12.5\ mol * 32\frac{g}{mol} + 12.5\ x\ 3.76\ mol * 28\ g/mol} = .06605$$

Appendix C: Additional Graphs

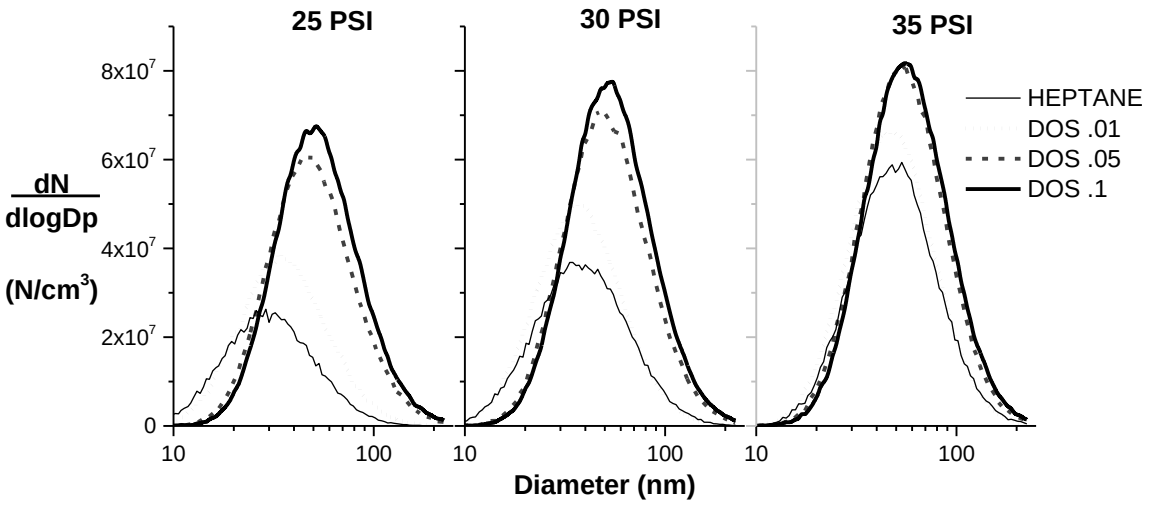

Appendix C Figure 1: Particle Distributions for DOS Solutions

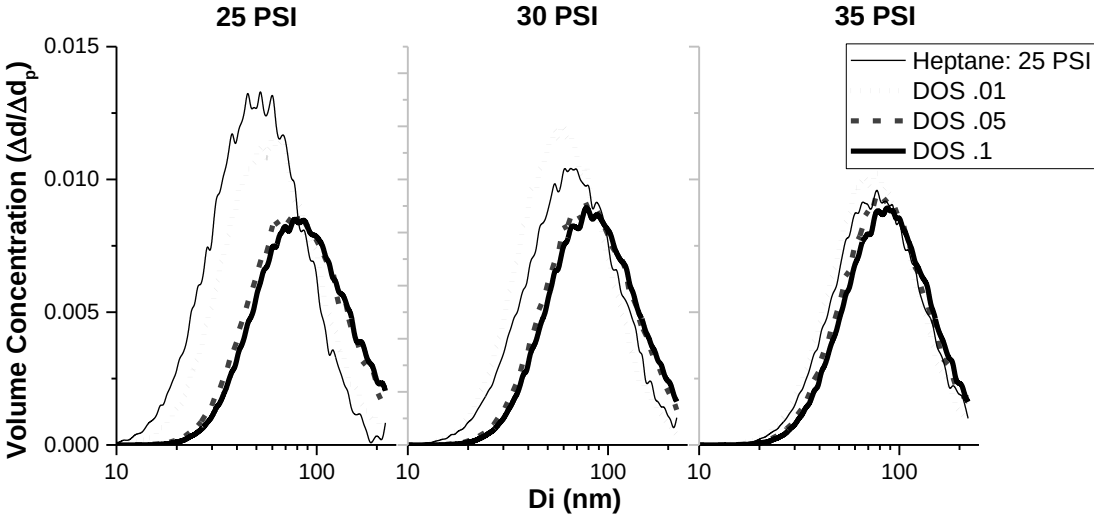

Appendix C Figure 2: Volume Distributions for DOS Solutions

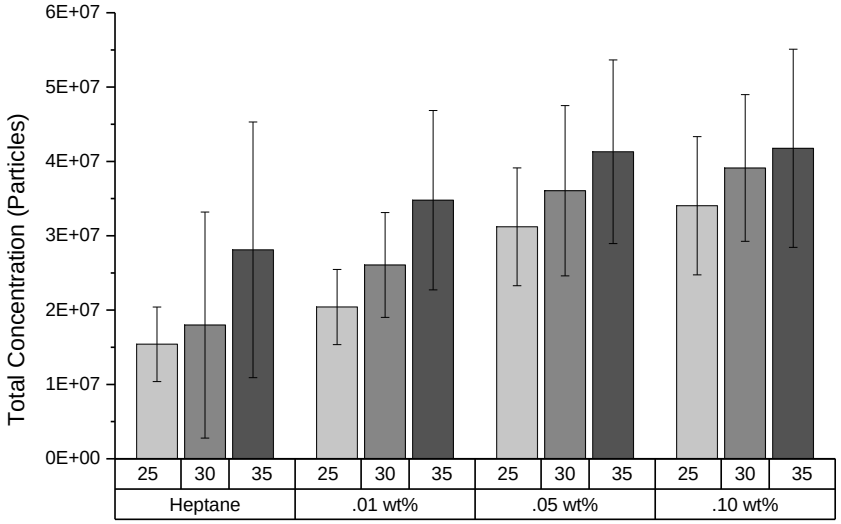

Appendix C Figure 3: Total Concentration for each factor-level combination for the four DOS/n-heptane solutions

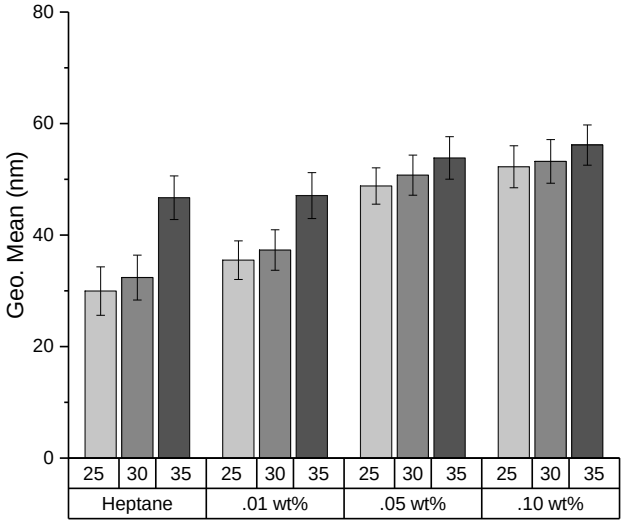

Appendix C Figure 4: Geometric Mean for the twelve factor-level combinations (DOS/n-heptane solutions)

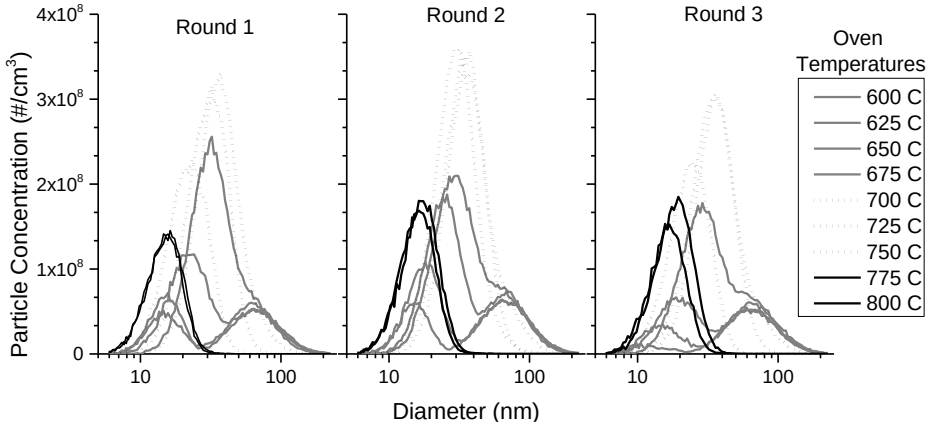

Appendix C Figure 5: Particle Distributions for the Three Rounds of Furnace Sweeps